Continuous, Dynamic and Steady State Simulation of the Reflux Classifier Using a Segregation-Dispersion Model

N.H. Syed, J.E., Dickinson, K.P. Galvin, R. Moreno-Atanasio*

[1]Centre for Advanced Particle Processing and Transport, University of Newcastle, Callaghan, NSW 2308, Australia

[*]*Corresponding author. Email:* roberto.moreno-atanasio@newcastle.edu.au

Abstract: A 2D continuous segregation-dispersion model incorporating a laminar-shear separation mechanism has been developed to describe the Reflux Classifier (RC). The RC, which consists of a fluidization zone, and a system of closely-spaced inclined channels, is now widely used to achieve gravity separation of a broad range of commodities. The narrow inclined channels promote the laminar-shear mechanism, leading to the selective shear-induced lift of low density particles, while allowing the fine and denser particles to deposit onto the inclined surfaces, and slide downwards. This mechanism allows a sharp density-based separation. The simulation results of this study have been validated using previously published experimental data. A total of 42 particle species were used in the simulations, corresponding to 6 different sizes and 7 different densities for each particle size, covering the particle size range of -2.0+0.125 mm. Simulation partition curves showed good agreement with the published experimental data, including the D_{50} and E_p values over the particle size range -2.0+0.25 mm. The model has also been tested to investigate the effect of high solid throughputs on the separation performance in the RC. The predictions of the fractional and cumulative ash % of the product and reject streams have been compared with the published experimental results demonstrating a good agreement and thus, the robustness of the model.

Keywords: continuum model, hindered settling, inclined channels, Reflux Classifier, resuspension, segregation-dispersion model.

1. Introduction

Increased interest in achieving an improved beneficiation of coal and minerals has led to the adoption of new technologies such as the Reflux Classifier (RC). The mechanisms governing the RC were first investigated by Galvin and co-workers (Galvin et al., 2002a, b; Doroodchi et al., 2004, 2006; Laskovski et al., 2006). The Reflux Classifier (RC) consists of a liquid fluidized bed with a set of parallel inclined channels located above the fluidization section (Laskovski et al, 2006), as shown in Fig. 1. The separation of particles within the fluidization section of the RC is similar to that achieved by liquid fluidized beds, governed by hindered settling, and the so-called phase inversion mechanism (Moritomi et al., 1982). Whereas, the inclined channels, which produce the Boycott Effect (Boycott, 1920; Galvin et al., 2002a, b), provide a large effective settling area. Within the inclined channels of the RC, the denser particle species settle onto the upward facing surfaces of the inclined channels, and slide downwards towards the fluidization section, while, the lower density particle species convey along the inclined channels, reporting as overflow (Galvin et al., 2002a, b; Amariei et al., 2014; Tripathy et al., 2015).

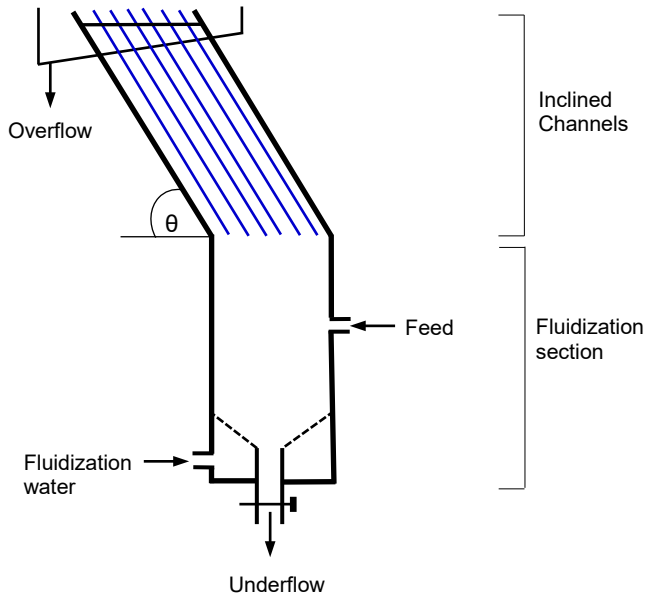

Fig. 1. Schematic diagram of the RC, comprising of a fluidization section and an inclined section.

Prior to 2009, the inclined channel spacing varied considerably, with values of 60 mm and 120 mm in different systems, and later narrower channels of 25 mm were used. A significant breakthrough was then achieved in 2009 through the introduction of closely spaced inclined channels (Galvin et al., 2009, 2010), with the channel spacing finally set at 6 mm. For coal, over the size range of -2.0+0.25 mm, the overall Ecart probable, or separation error, Ep, decreased from 0.15 for the wider inclined channels (Galvin et al., 2002a, 2005) down to about 0.06 for the closely spaced inclined channels in experiments (Galvin et al., 2010). The introduction of the closely spaced inclined channels led to the laminar-shear separation mechanism, and to the selective shear induced lift of coarse low density particles (Galvin et al., 2009, 2010; Galvin and Liu, 2011). This phenomenon allows fine dense particles to settle on the inclined surfaces. Therefore, the overflow mainly consists of fine and coarse particles of low density. The accumulation of the fine, denser particles in the fluidization section of the RC promotes an autogenous dense media to form, promoting the phase inversion mechanism, and hence upwards displacement of the larger and lower density particles from the lower fluidization zone. Widespread adoption of the RC followed from the introduction of the laminar shear mechanism, with improved performance in both fine coal and fine iron ore beneficiation (Galvin et al, 2010; Amariei et al., 2014).

The sedimentation and segregation of particle species of a multicomponent system in different sections of the RC for a continuous process has not been studied theoretically in detail. Whereas, in the liquid fluidized beds considerable experimental and theoretical research has been undertaken on single, binary and multicomponent systems. This research has led to descriptions of the segregation, dispersion, mixing, layer inversion and sedimentation phenomena (Pruden and Epstein, 1964; Kennedy and Bretton, 1966; Moritomi et al., 1982; Van Duijn and Rietema, 1982; Asif and Petersen, 1993; Di Felice, 1995; Asif, 1997, 1998; Chen et al., 2002; Rasul et al., 2002; Asif, 2004; Ramirez and Galvin, 2005; Galvin et al., 2006; Patel et al., 2008).

Kennedy and Bretton (1966) proposed for the first time a segregation-dispersion model to study the dispersion in liquid fluidized beds under batch conditions (Asif and Petersen, 1993, Asif, 1997, Ramirez and Galvin, 2005). The model accurately predicted the movement and separation of particle species observed in experiments,

showing that larger particles settle towards the bottom of the bed while smaller particles move towards the top of the bed (Kennedy and Bretton, 1966; Asif, 1998). According to the authors (Kennedy and Bretton, 1966), the transport of solid particles was the result of the combination of dispersion and segregation processes. The Kennedy and Bretton (1966) approach has been used as the basis of most of the models developed after this for liquid fluidized beds (Juma and Richardson, 1983; Asif and Petersen, 1993, Asif, 1997, Ramirez et al., 2005; Galvin et al., 2006; Patel et al., 2008)

This paper is concerned with developing a model of the RC for a continuous process based upon the principles of segregation and dispersion in liquid fluidized beds (Kennedy and Bretton, 1966), coupled with an appropriate hindered settling model that provides at least some account of phase inversion. The model also incorporates the mechanism of shear induced lift to simulate the resuspension of particle species within the inclined channels of the RC.

2. Segregation-Dispersion model

2.1 Theoretical development

The segregation-dispersion model used to simulate the RC is based upon the Kennedy and Bretton (1966) approach. Accordingly, the movement of the particle species within the RC is based upon the fact that the particle species possess a net particle flux, J_i, relative to the vessel at a specific height within the vessel. The net flux of a particle species relative to the vessel comprises dispersion and segregation fluxes (Kennedy and Bretton, 1966; Juma and Richardson, 1983; Ramirez and Galvin, 2005; Patel et al., 2008). The mathematical expression of this flux balance is given as,

$$J_i = \phi_i v_{p,i} = - D_{p,i} \frac{\partial \phi_i}{\partial y} + \phi_i v_{seg,i} \quad (1)$$

where the subscript i refers to single particle species having a specific size and density, $v_{p,i}$ is the velocity of a particle species relative to the vessel, $D_{p,i}$ the dispersion coefficient, $v_{seg,i}$ the segregation velocity and ϕ_i the volume fraction of the particle

species. The terms $\frac{\partial \phi_i}{\partial y}$, $-D_{p,i}\frac{\partial \phi_i}{\partial y}$ and $\phi_i v_{seg,i}$ represent the local concentration gradient, the dispersion flux and the segregation flux of the particle species i, respectively.

In a continuous process, the total volume flux, v_N, through the system depends upon the zones below and above the feed points. Therefore, at the feed point and above, the total volume flux is given as,

$$v_N = v_{fs} + J_f - J_u = v_f \phi_f + \sum \phi_i v_{p,i} \quad (2)$$

and below the feed point the total volume flux is expressed as,

$$v_{fs} - J_u = v_f \phi_f + \sum \phi_i v_{p,i} \quad (3)$$

where J_f is the total volumetric feed flux, J_u is the underflow flux, v_{fs} the fluidization flux, v_f the interstitial fluid velocity and ϕ_f the volume fraction of liquid or the voidage.

In the RC, due to the inclination of the channel, the amount of material circulating through the system is expected to depend on the horizontal coordinate, hence a 2D model was developed. The x-component is taken as the component normal to the inclined surfaces and y-component is taken as the tangential component, as schematically shown in Fig. 2.

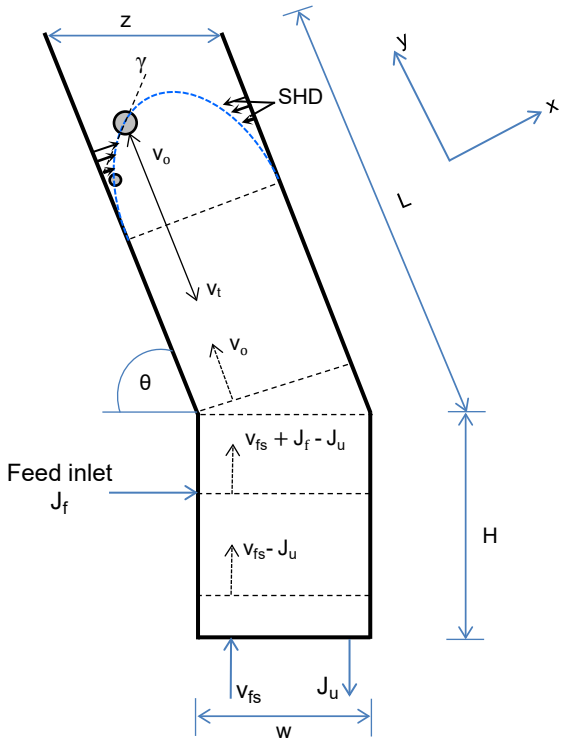

Fig. 2: Schematic diagram of the computational domain showing flux movement and parabolic profile of the liquid into the system.

Now, the net fluxes of particle species relative to the vessel in the x and y directions are given as,

$$J_{x,i} = \phi_i v_{p\_x,i} = - D_{p,i} \frac{\partial \phi_i}{\partial x} + \phi_i v_{seg\_x,i} \quad (4)$$

$$J_{y,i} = \phi_i v_{p\_y,i} = - D_{p,i} \frac{\partial \phi_i}{\partial y} + \phi_i v_{seg\_y,i} \quad (5)$$

The segregation velocity ($v_{seg,i}$) in terms of x and y components is given as,

$$v_{seg\_x,i} = v_{slip\_x,i} + v_{f\_x} \quad (6)$$

$$v_{seg\_y,i} = v_{slip\_y,i} + v_{f\_y} \quad (7)$$

where $v_{slip\_x,i}$ and v_{f_x} are the slip velocity of the particle species relative to the fluid and interstitial fluid velocity in the x direction respectively. Similarly, $v_{slip\_y,i}$ and v_{f_y}

are the slip velocity of the particle species relative to the fluid and interstitial fluid velocity in the y direction respectively. Within the inclined channel, in the normal direction, the sedimentation of a particle species is equivalent to conventional batch settling (Nguyentranlam and Galvin, 2001; Doroodchi et al., 2004). Therefore, the interstitial fluid velocity normal to the plane is negligible compared to the slip velocity in the same direction (Nguyentranlam and Galvin, 2001), especially under dilute conditions.

In order to calculate the slip velocities of the particle species, the hindered settling model proposed by Asif (1997) has been used. This model is a modified version of the Richardson and Zaki model (1954), and predicts a relative particle velocity on the basis of density of particle species and bulk density of the bed (Asif, 1997; Galvin et al. 1999; Patel et al., 2008). The model is represented as,

$$v_{slip,i} = v_{t,i} \left(\frac{\rho_i - \rho_{sus}}{\rho_i - \rho_f} \right)^{n_i - 1} \tag{8}$$

where v_t is the particle terminal settling velocity, which depends on particle size. Therefore, particle size is implicitly included in the simulations through the use of the particle terminal velocity which is one of the input parameters in the model. The suspension density, ρ_{sus}, is given as,

$$\rho_{sus} = \sum \phi_i \rho_i + (1 - \sum \phi_i) \rho_f \tag{9}$$

where ρ_i is the density of the particle species i and ρ_f the fluid density. If there is a single particle species, the hindered settling model of Asif (1997) will take the form of the Richardson and Zaki (1954) model.

When the value of the suspension density exceeds the value of the particle density, the normalised density becomes negative. This means we cannot apply the empirical exponent directly (Eq. 8). Rather, in this situation, we apply the empirical exponent to the absolute value of the normalised density difference to obtain the hindered settling factor. The hindered settling factor is then multiplied by -1, indicating a reversal in the direction of the slip velocity. Under these conditions, a given particle with a low density

with respect to the surrounding medium, will migrate in the upwards direction. At a fundamental level, this also implies the particle migrates upwards relative to the local fluid.

Therefore, Eq. (8) takes the form,

$$v_{slip,i} = v_{t,i}\, \ell \left| \left(\frac{\rho_i - \rho_{sus}}{\rho_i - \rho_f} \right) \right|^{n_i - 1} \tag{10}$$

where the directional parameter, ℓ=1, if $\left(\frac{\rho_i - \rho_{sus}}{\rho_i - \rho_f} \right)$ is greater than or equal to zero, and ℓ = -1, if $\left(\frac{\rho_i - \rho_{sus}}{\rho_i - \rho_f} \right)$ is less than zero. Thus, the slip velocity model in the x (normal to the plane) and y (parallel to the plane) directions becomes,

$$v_{slip\_x,i} = \left[v_{t,i}\, \ell \left| \left(\frac{\rho_i - \rho_{sus}}{\rho_i - \rho_f} \right) \right|^{n_i - 1} \right] \cos\theta \tag{11}$$

$$v_{slip\_y,i} = \left[v_{t,i}\, \ell \left| \left(\frac{\rho_i - \rho_{sus}}{\rho_i - \rho_f} \right) \right|^{n_i - 1} \right] \sin\theta \tag{12}$$

Now the interstitial fluid velocity inside the RC in the y direction can be calculated separately at two different locations, taking into account the total net flux at each location. The interstitial fluid velocity at the feed point and above the feed point is calculated as,

$$v_{f\_y} = \frac{(v_{fs} + J_f - J_u - \sum \phi_i v_{p,i})}{(1 - \sum \phi_i)} \tag{13}$$

Below the feed point, the interstitial fluid velocity is calculated as,

$$v_{f\_y} = \frac{(v_{fs} - J_u - \sum \phi_i v_{p,i})}{(1 - \sum \phi_i)} \tag{14}$$

Since the channel spacing is narrow, the flow is assumed to be laminar, and hence the net flow (particles plus water) has a parabolic profile. This assumption was later validated by calculating the Reynolds number of the fluid within the inclined channel,

and confirming the magnitude to be well below 2100. For simplicity, the superficial velocity tangential to the plane, v_o, entering into the inclined channel is assumed to adopt the parabolic shape instantly. Thus,

$$v_o = \frac{6\, v_N\, x_p}{z}\left(1 - \frac{x_p}{z}\right) \tag{15}$$

where z is the channel spacing and x_p the position of the particle within the inclined channel.

At steady state the interstitial fluid velocity within the inclined channel, parallel to the plane is given as,

$$v_{f\_y} = \frac{(v_o - \sum \phi_i v_{p,i})}{(1 - \sum \phi_i)} \tag{16}$$

Since, the model is developed for a continuous process, the amount of material discharging from the bottom of the system as underflow for each species i is calculated as,

$$J_{su,i} = \phi_{su,i}\ J_u \tag{17}$$

where $\phi_{su,i}$ is the solid volume fraction at the bottom of the RC and $J_{su,i}$ the solid flux.

The boundary condition at the bottom of the system is equal to the flux emerging from the system. Similarly, we set the concentrations of the particles species equal to zero at the top layer of the system. The boundary conditions are given as:

$$z = z_{max} \qquad \phi_i = 0 \tag{18}$$

$$z = 0 \qquad J_{y,i} = J_u \tag{19}$$

A mechanism of shear-induced lift has been introduced in the segregation-dispersion model of the RC to accommodate the effects of the high shear rate that arises when closely spaced channels are used. The shear rate inside the inclined channels is maximum near the walls and approaches zero at the centre of the channel. The shear

rate causes shear-induced lift or shear-induced self-diffusion, which involves the resuspension of relatively low density particles (Leighton and Acrivos, 1986, 1987a; Zhang and Acrivos, 1994).

Eckstein, Bailey & Shapiro (1977), and Leighton & Acrivos (1987b) conducted experiments to examine the shear-induced self-diffusion phenomena. They proposed the diffusion coefficient is proportional to γr_i^2, where γ is the shear rate and r_i the radius of the particle species (Leighton and Acrivos, 1987a). For relatively fine particles, this resuspension can be described as shear-induced hydrodynamic dispersion (SHD) while for coarser particles of higher Reynolds number inertial lift is involved (King and Leighton, 1997).

Within the inclined channels the particles experience a strong and distinct shear rate at the wall due to the laminar flow profile. In turn this shear rate promotes the resuspension of the particles. For example, at low Reynolds numbers Leighton and Acrivos (1986) observed so-called “viscous resuspension” arising from the phenomenon of hydrodynamic diffusion (Zhang and Acrivos, 1994; Krishnan and Leighton Jr, 1995; Schroen et al., 2017). For much larger particles, inertial lift prevails as described by King and Leighton (1997). In our model we have sought a simple empirical approach to describe the mechanism for lift, consistent with the segregation-dispersion model that underpins the entire model. Therefore, we have configured a description of the dispersion coefficient, dependent on the shear rate and particle radius squared (Leighton and Acrivos, 1986; Schroen et al., 2017), borrowing from the form used for particles at low Reynolds numbers. We have assigned a coefficient, $C_o=4.8x10^4$, to achieve a degree of lift consistent with the experimental results. Future work will focus on the dimensionless groups that underpin this value in order to produce a more general description of the lift force. We suspect the coefficient is directly related to the drag coefficient, which of course depends on the particle Reynolds number (Galvin and Liu, 2011).

The mechanism of resuspension has been implemented as a contribution to the dispersion in the segregation-dispersion model of the RC, as shown in Fig. 2. To be effective, the mechanism requires a significant shear rate, which is best generated

using closely spaced inclined channels typically less than 6 mm in width. So the modified dispersion coefficient, D_i , normal to the plane within the inclined channel is given as,

$$D_i = C_o \gamma (r_i)^2 \qquad (20)$$

For a typical value of shear rate of 9 s^{-1}, Eq. 20 yields values of the dispersion coefficients in the range 0.0038 to 0.312 m^2/s. The magnitude of this dispersion coefficient is significantly larger than the isotropic value adopted elsewhere in the system. In Eq. (20), r_i is radius of the particle species i and γ (Galvin and Liu, 2011) is given as,

$$\gamma = \frac{6\, v_N}{z}\left(1 - \frac{2\, x_p}{z}\right) \qquad (21)$$

Fig. 2 shows the schematic representation of SHD, which is a maximum near the walls of the channel and minimum at the centre of the channel.

2.2 Implementation of the model

In order to implement the model, the whole fluidized and inclined sections of the RC were discretized into equally spaced shells and elements in the x and y directions as shown in Fig. 3. The whole domain was divided into 100 shells and 11 elements. The element nearest to the left is the element number 1 while the element nearest to the right surface of the inclined channel is element number 11.

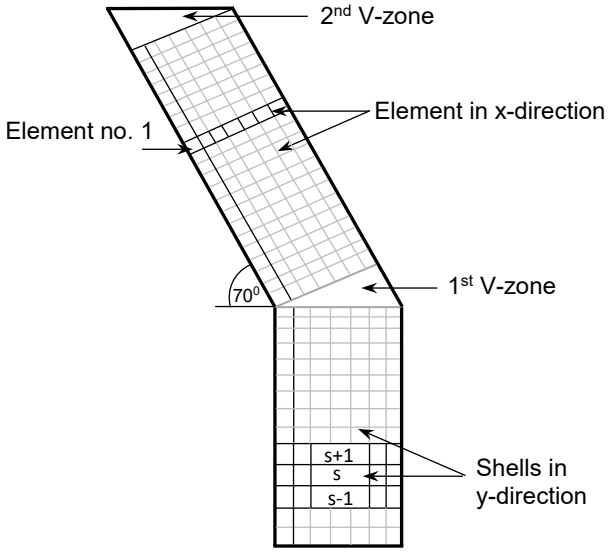

Fig. 3: Schematic representation of the computational domain showing the shells and elements in the system.

In Fig. 3, two minor zones termed V-zones are shown. One V-zone is at the start of inclined channel and the second is at the top of the inclined channel. The effect of the V-zones is expected to be very small due to the fact that the inclined channel is very narrow and very long compared to the dimensions of the V-zones.

Patel et al. (2008) have described the one-dimensional shell modelling approach adopted here. The volume fractions of the individual particle species in each element and shell were obtained from the simulations. Then, the slip velocities of particle species in the x and y directions were evaluated using Eq. (11) and (12). The interstitial fluid velocity at the feed inlet and above was calculated using Eq. (13). Similarly, the interstitial fluid velocity below the feed inlet was calculated using Eq. (14). The segregation velocities in the x and y directions were calculated using Eq. (6) and (7). After that, the segregation flux was calculated using Eqs. (6) and (7). For particle species whose segregation flux was positive, a corresponding volume of material equal to $\phi_i v_{seg\_y,i} A \Delta t$ moved from the current shell to the upper shell. In contrast, for the particle species whose segregation flux was negative, a volume of material equal to $\phi_i v_{seg\_y,i} A \Delta t$ moved in the downwards direction from the current shell.

In the same way, for the dispersion flux in the y direction, when the concentration gradient had a negative value, then the dispersion flux became positive and a calculated volume of material moved from the current shell to the upper shell. Whereas, when the concentration gradient was positive, the dispersion flux term became negative and the particle species moved from the upper shell to the current shell. The movement of material in the x direction took place from one element to another following the same algorithm described for the y direction.

The value of the dispersion coefficient that allowed the simulations to closely match the experimental results, obtained as a fitting parameter, was set equal to 0.00030 m^2/s. This value is within the typical range found in the literature (Juma and Richardson, 1983; Asif and Petersen, 1993; Asif, 1998; Ramirez and Galvin, 2005; Patel et al., 2008) and hence is physically meaningful. This value was used in the vertical and horizontal directions in the fluidization section of the RC.

Similarly, in the inclined channel, a dispersion coefficient of 0.00030 m^2/s (as a fitting parameter) was applied in the y-direction (parallel to the inclined channel). In the x-direction (normal to the inclined channel), Eq. (20) was used in order to simulate the effect of shear-induced hydrodynamic dispersion (SHD).

In order to simulate the RC for realistic time scales we have only considered the width of a single channel and have modelled the fluid flow accordingly. Thus, a flat liquid profile (Cornelissen, et al., 2007, Reddy, et al., 2009) typical of the vertical section of a multichannel system was used to simulate particle transport in the fluidization section. However, given the narrow spacing of the channel (6 mm), a parabolic fluid profile was considered in the inclined section. Furthermore, as shown above, the dispersion coefficient was isotropic in the fluidization region while it was anisotropic, Eq. (20), in the inclined channel. Therefore, the model has been configured physically to represent a full-scale RC with multiple inclined channels.

2.3 Calculation of particle terminal velocity

The Zigrang and Sylvester (1981) equation was used to calculate the Reynolds number of the particle, Re_t,

$$Re_t = \left[(14.51+1.83\left(g\times\left(\rho - \rho_f\right)\rho_f\right)^{0.5} \frac{d^{1.5}}{\mu}\right)^{0.5} - 3.81\right]^2 \quad (22)$$

where μ is the viscosity of the fluid. After obtaining the value, Re_t, the particle terminal settling velocity, required in Eq. (8), was calculated using Eq. 23,

$$Re_t = \frac{\rho_f v_{t,i} d}{\mu} \quad (23)$$

A fixed value of n = 3.2 was taken during the simulations as the Richardson and Zaki (1954) exponent in Eq. 8, based upon average values for the system of particles (which can be considered as a fitted parameter).

2.4 Analysis of partition curves

Partition curves describing the partition number, P, as a function of the particle relative density, RD, were obtained and used to validate the findings from the computer simulation using published experimental results. The partition curves describe the probability of particles of a given density reporting to either the overflow or underflow. If the value of P is 0.5 then RD = D_{50}, where, the $D_{50,}$ represents the relative density of a particle species having 50% probability of reporting either to the overflow or the underflow. The data points have been fitted by using the function:

$$P = \frac{1}{1+\exp\left(-\frac{\ln 3\,(D_{50} - RD)}{E_p}\right)} \quad (24)$$

where the Ecart probable, Ep, represents the sharpness of the separation. The equation for calculating the Ep is given as,

$$Ep = \frac{D_{75} - D_{25}}{2} \quad (25)$$

where D_{75} and D_{25} represent the relative densities of the particle species that have 75% and 25% probability of reporting to the overflow, respectively. If the value of the Ep is close to zero, then the separation is considered to be very efficient. Whereas, if the value of the Ep is approaching towards one or higher, then the separation would be considered to be very poor.

3. Simulation details

An in-house computer code, named SDM-RC-Continuum, was developed using Fortran 77. The simulations were performed for a multicomponent system and the results validated using the experimental results of Galvin et al. (2010). The dimensions of the system were taken as 1 m for the height of the fluidization section and 1 m for the length of the inclined channel. The vertical section had the cross sectional area of 6 mm x 6 mm. Computations were performed on just one inclined channel having an inclination of 70°. The feed inlet point was considered to be at a height of 0.7 m (shell no. 35) and the inclined channel commenced at 1 m (shell no. 51).

Here, 42 particle species having 7 different densities and 6 different sizes were selected. The particle species were selected in order to match the size ranges, -2.0+1.40 mm, -1.40+0.70 mm, -0.70+0.50 mm, -0.50+0.35 mm, -0.35+0.25 mm and -0.250+0.125 mm, according to the published experimental results of Galvin et al. (2010). The properties of the particle species, such as, size, density, terminal settling velocity and terminal Reynolds number, used in the simulations, are shown in Table 1.

During the first set of simulations, a total solid flux of 0.0011 m^3/m^2s and water flux of 0.0075 m^3/m^2s, together forming a total slurry flux of 0.0086 m^3/m^2s was introduced into the system as feed. The fluidization velocity and underflow flux were kept at 0.0018 m/s and 0.00075 m^3/m^2s during the simulations, respectively. The calculated value of the Reynold's number inside the inclined channel was 54.

According to the Wen and Yu (1966) equation, when using the Sauter mean particle diameter and mean values of particle density (Li et al., 2005), the minimum fluidization

velocity required was 0.0007 m/s. The solid volume fraction obtained using Ergun's (1952) equation at the minimum fluidization velocity was 0.66. Hence, the RC was operated with a velocity close to the minimum fluidization value in the vicinity of the base of the RC.

In contrast, by taking the arithmetic mean values of particle size and density, the value of the minimum fluidization velocity was 0.0020 m/s for which the solid volume fraction was 0.62. Please note that the minimum fluidization velocity required for the smallest and lightest particle species (0.19 mm and 1275 kg/m^3) was 0.0001 m/s. In contrast, for the largest and heaviest particle species (1.70 mm and 25 kg/m^3) the minimum fluidization velocity required was 0.018 m/s.

Table 1: Particle properties selected for simulations.

Particle size (mm)	Particle density (kg/m^3)	Particle Reynolds number	Terminal settling Velocity (m/s)
1.70	1275	125.2	0.074
1.70	1350	145.6	0.086
1.70	1450	170.0	0.100
1.70	1600	202.6	0.120
1.70	1800	240.8	0.140
1.70	2050	283.2	0.170
1.70	2500	349.4	0.210
1.00	1275	44.3	0.044
1.00	1350	52.1	0.052
1.00	1450	61.7	0.062
1.00	1600	74.5	0.075
1.00	1800	89.8	0.089
1.00	2050	106.9	0.110
1.00	2500	133.7	0.130
0.60	1275	14.8	0.025
0.60	1350	17.7	0.029
0.60	1450	21.3	0.036
0.60	1600	26.2	0.044
0.60	1800	32.1	0.054
0.60	2050	38.8	0.065
0.60	2500	49.5	0.083
0.42	1275	6.5	0.015

0.42	1350	7.8	0.019
0.42	1450	9.5	0.023
0.42	1600	11.9	0.028
0.42	1800	14.8	0.035
0.42	2050	18.1	0.043
0.42	2500	23.5	0.056
0.30	1275	2.8	0.0094
0.30	1350	3.4	0.012
0.30	1450	4.3	0.014
0.30	1600	5.4	0.018
0.30	1800	6. 8	0.023
0.30	2050	8.4	0.028
0.30	2500	11.1	0.037
0.19	1275	0.8	0.0045
0.19	1350	1.1	0.0055
0.19	1450	1.3	0.0069
0.19	1600	1.7	0.0089
0.19	1800	2.2	0.011
0.19	2050	2.7	0.014
0.19	2500	3.7	0.019

4. Results and Discussion

4.1 Model validation

Simulations were performed to obtain model predictions. The data obtained through simulations was used to produce six partition curves representing the narrow size fractions, -2.0+1.40 mm, -1.40+0.70 mm, -0.70+0.50 mm, -0.50+0.35 mm, -0.35+0.25 mm and -0.250+0.125 mm. The partition curves are plotted versus particle relative density in Fig. 4a for the six size fractions considered in the simulations. The partition curves show the typical shape of a logistic function as they trend to 1 and 0 for low and high values of the relative density, respectively. In addition, when the particle size increases, the curves shift towards the left indicating that lower particle densities emerge from the system via the overflow. A similar trend was observed in the experimental work by Galvin et al. (2010). For comparison of the model predictions

and the experimental results, partition curves obtained by Galvin et al. (2010) through experimental work have been used and are shown in Fig. 4b.

The comparison of Fig. 4a and b demonstrates good agreement between the model predictions and the experimental results for the particle size range -2.0 + 0.25 mm. However, the main difference can be seen in the behaviour of the fine particles representing the size range -0.250 + 0.125 mm, for which a larger tendency to report to the overflow has been observed in the simulation results compared to the experiments. The discrepancy in this size fraction reflects the sensitivity of the model in dealing with fine particles in the inclined channel. For example, the sliding of the sediment influences the fluid velocity profile and hence shear rate at the inclined surface. The precise cause of the discrepancy remains unclear, and will constitute future work.

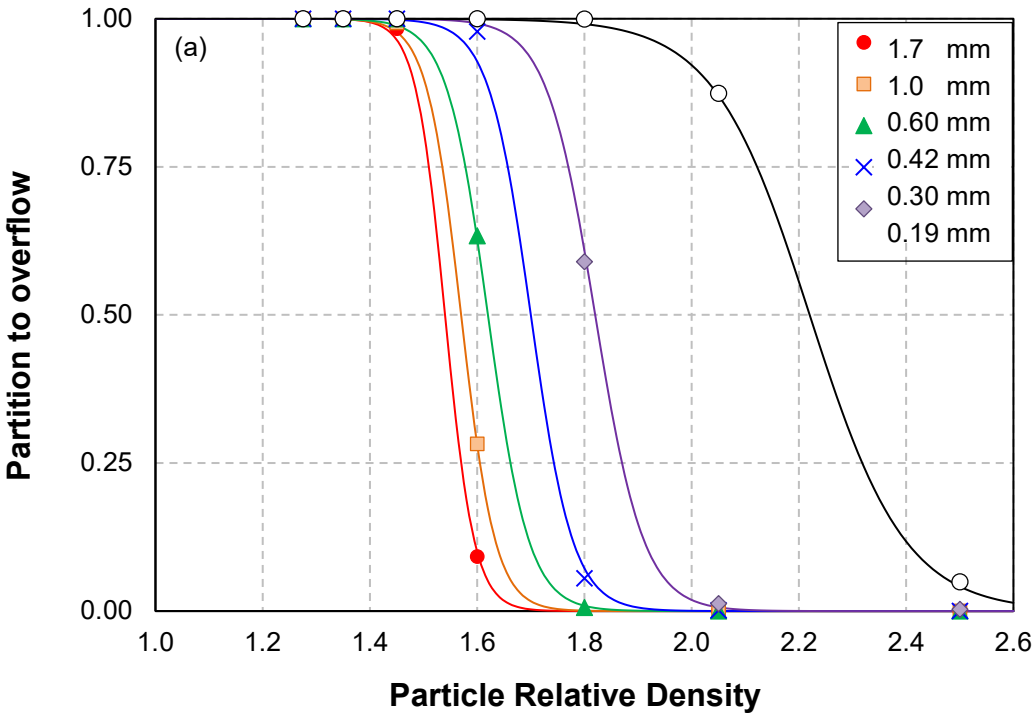

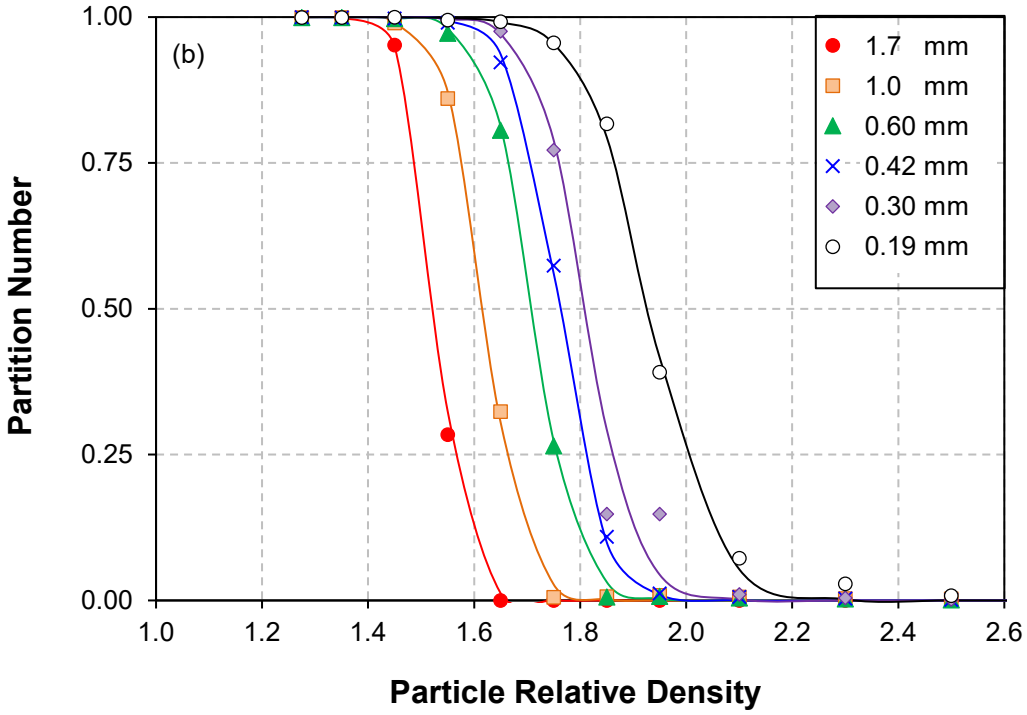

Fig. 4. Partition curves for the average size fractions 1.70 mm, 1.0 mm, 0.60 mm, 0.42 mm, 0.30 mm and 0.19 mm, representing narrow size fraction -2.0+1.40 mm, -1.40+0.70 mm, -0.70+0.50 mm, -0.50+0.35 mm, -0.35+0.25 mm and -0.250+0.125 mm respectively: (a) Partition curves predicted by the model through simulations; (b) Partition curves obtained from the experimental results of Galvin et al. (2010).

Fig. 5 shows a comparison of the overall partition curve versus particle relative density for the particle size range -2.0 +0.250 mm obtained through the model predictions and the experimental results of Galvin et al. (2010). The solid circles and hollow squares correspond to the model predictions and the experimental results, respectively. The overall D_{50} and Ep values for the model predictions are 1.65 and 0.070, and for the experiments are 1.68 and 0.065, respectively. The model predictions are in good agreement with the experimental results within the size range -2.0 +0.250 mm.

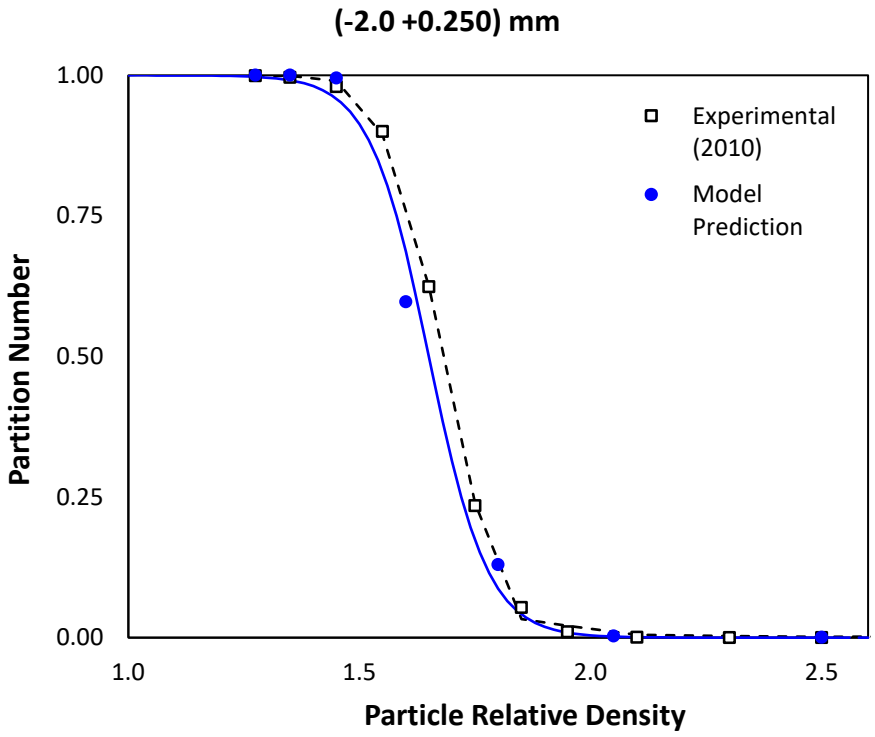

Fig. 5. Overall partition curves for the particle size range -2.0 +0.25 mm. The dashed curve represents the experimental results and the continuous curve represents the model predictions.

In order to compare the model predictions and the experimental results (Galvin et al., 2010), the D_{50} values have been plotted as a function of the particle size, shown in Fig. 6. The D_{50} values were derived from the partition curves obtained through model predictions and the experimental (Galvin et al., 2010) results. In Fig. 6, the dashed line with open squares represents the experimental results while the continuous line with filled circles represents the model predictions. The model predictions show a decrease in the D_{50} values with increase in particle size, similar to the experimental results. The main difference between the predicted D_{50} values and the experimental results is observed for the fine particle species.

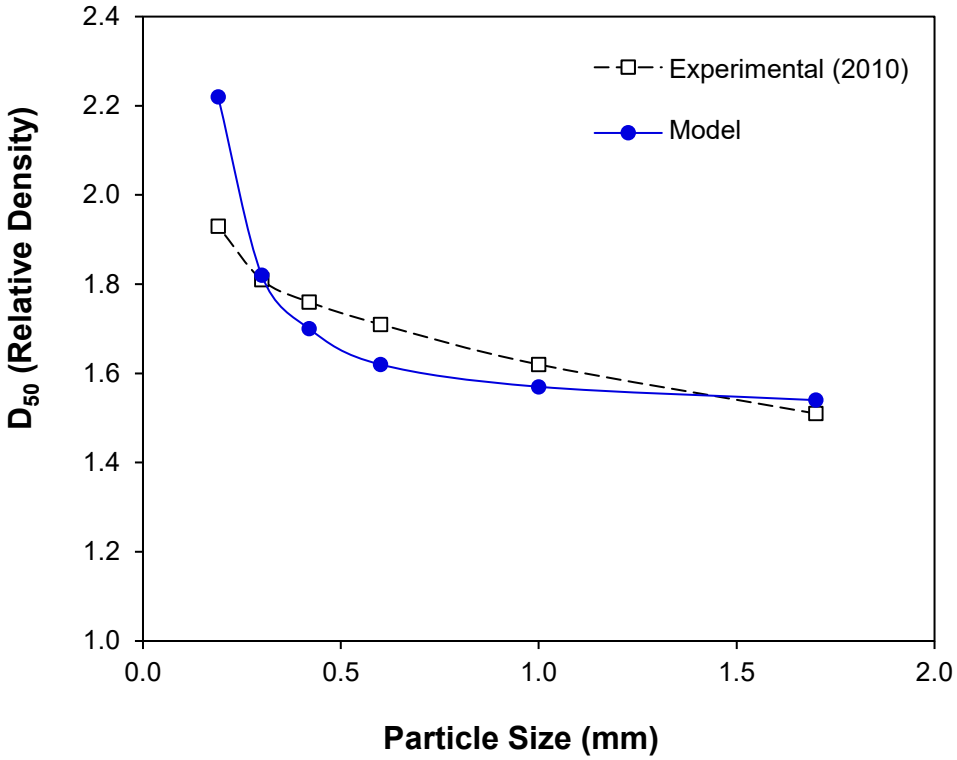

Fig. 6. The separation relative density, D_{50}, is shown as a function of particle size. A comparison between the D_{50} values, derived from the partition curves obtained through the model predictions and the experimental results of Galvin et al. (2010), has been demonstrated.

Similarly, Fig. 7 shows a comparison between the Ep values of the model predictions and the experimental results of Galvin et al. (2010) plotted as a function of particle size. The Ep values obtained using the simulations decreased with increasing particle size. However, it was observed that the Ep value increased slightly from 0.041 for a particle size of 0.42 mm to 0.042 for a particle size of 0.60 mm and then decreased to 0.032 and 0.026 for particle sizes of 1.0 and 1.7 mm, respectively. Overall, the model predictions and the experimental results showed good agreement.

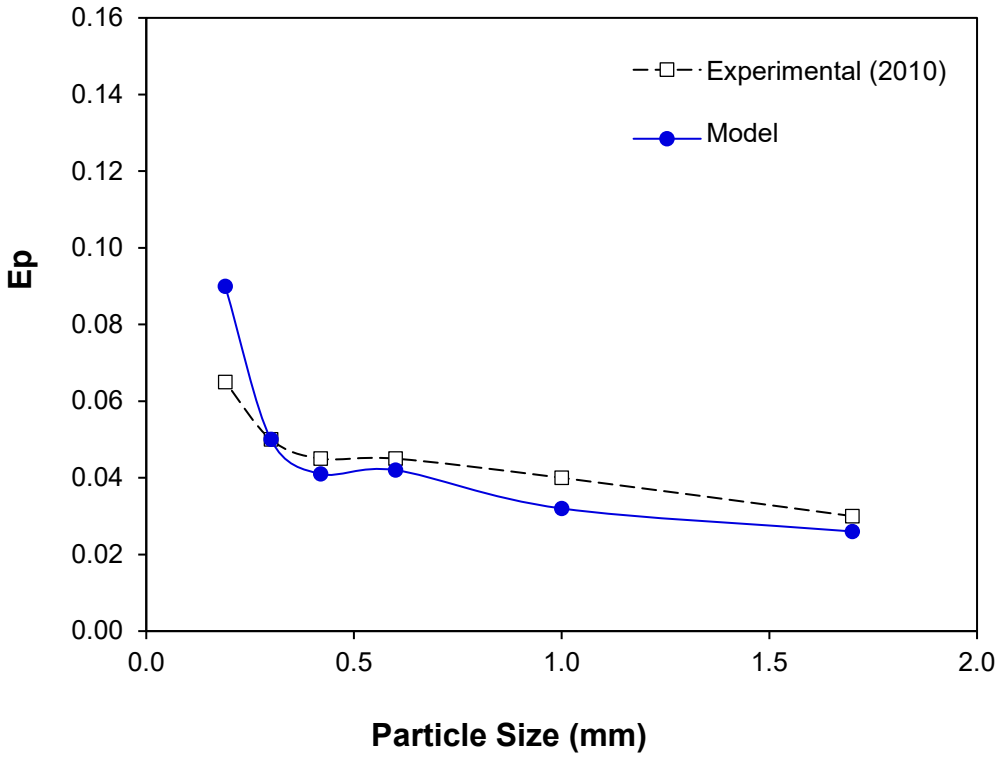

Fig. 7. The Ecart probable error, Ep, is shown as a function of particle size. A comparison between the Ep values, derived from the partition curves obtained through the model predictions and the experimental results of Galvin et al. (2010) has been demonstrated.

The model predictions have also been used to find the fractional and cumulative ash % for the feed, product and reject streams. The results are listed in Table A1 for a solid throughput of 6.3 t/m^2h (~0.0011 m^3/m^2s) and compared with the analysis of experimental results of Galvin et al. (2010), shown in Table A2. A graphical comparison of the model predictions and the experimental results for mass and ash fraction in the product and reject streams have been shown in Figures 8 and 9, respectively.

Fig. 8 shows a comparison of mass fraction in the product and reject streams of the model predictions and the experimental results of Galvin et al. (2010). The model predictions show a very good agreement with the experimental results.

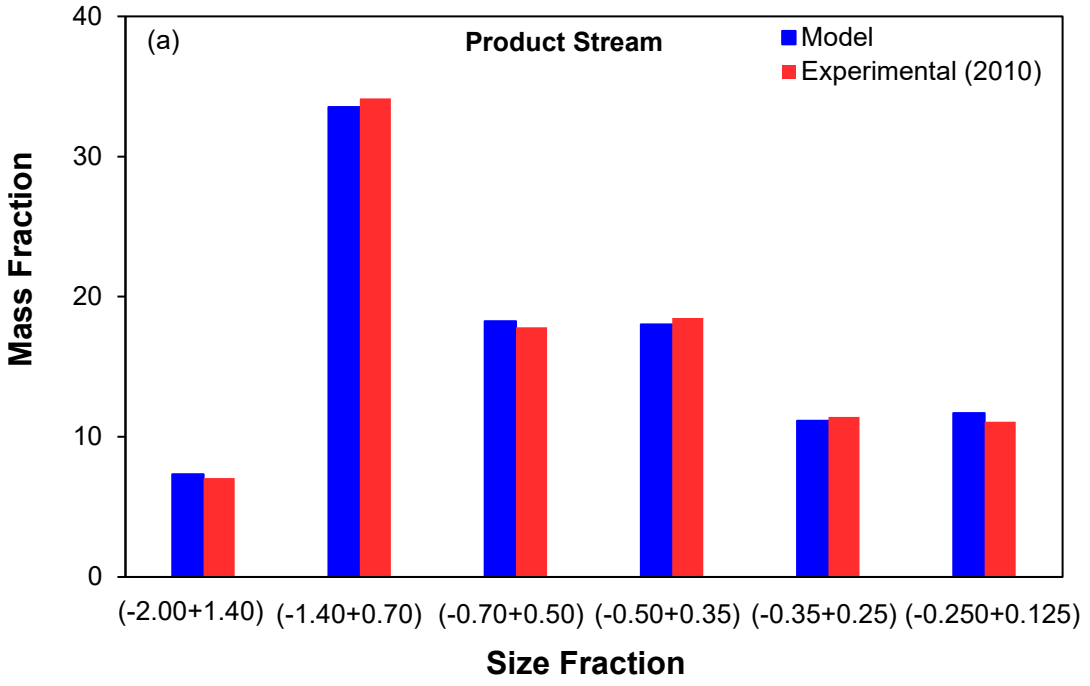

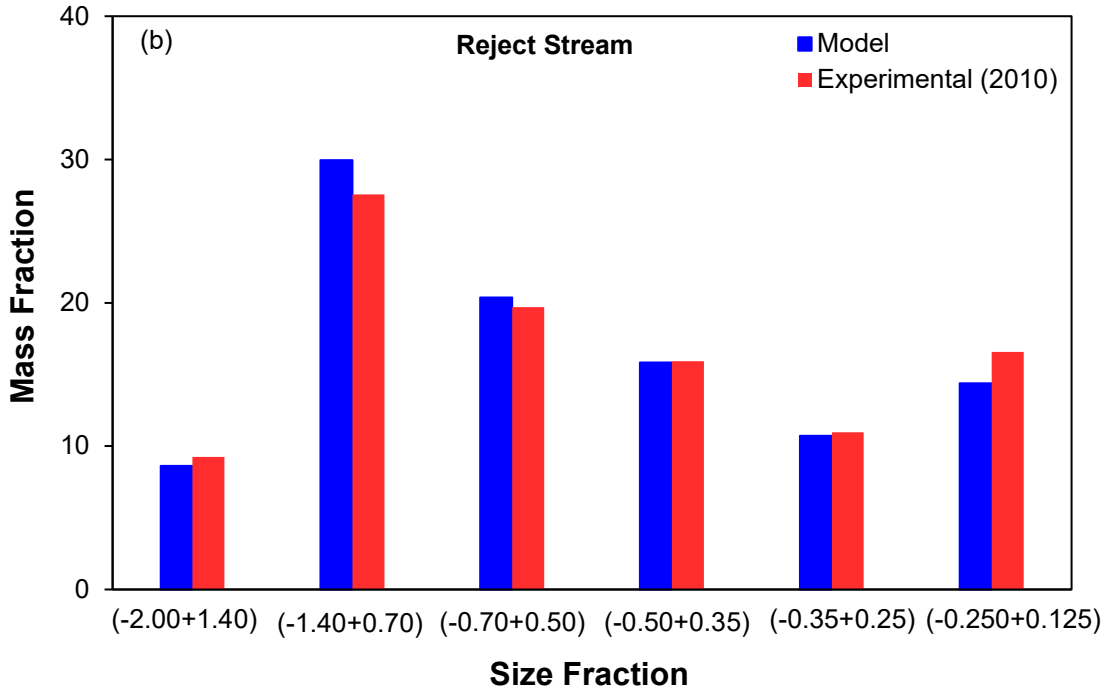

Fig. 8. Comparison of mass fraction in the feed and reject streams obtained through the analysis of model predictions and the experimental results of Galvin et al. (2010): (a) Product stream; (b) Reject stream.

Fig. 9 shows a comparison of ash % in the product and reject streams of the model predictions and the experimental results of Galvin et al. (2010). The ash % was obtained by using the correlation (Galvin, 2009),

$$RD = 0.014A+1.229 \quad (26)$$

where RD represents the relative density and A the ash %. Overall, the analysis of the ash % in the feed and reject stream obtained from the model predictions and the experimental results are in a good agreement. However, in the product stream for particle size fraction -0.250+0.125 mm the difference in ash % between the model prediction and the experimental results is large. This difference is due to fact that the fine and dense particle species move out from the system as an overflow at a higher rate in the simulations than in the experimental work. Since the dense species move out as overflow, the ash % in the product stream, predicted by the model, is greater than the ash % in product stream obtained from experiments.

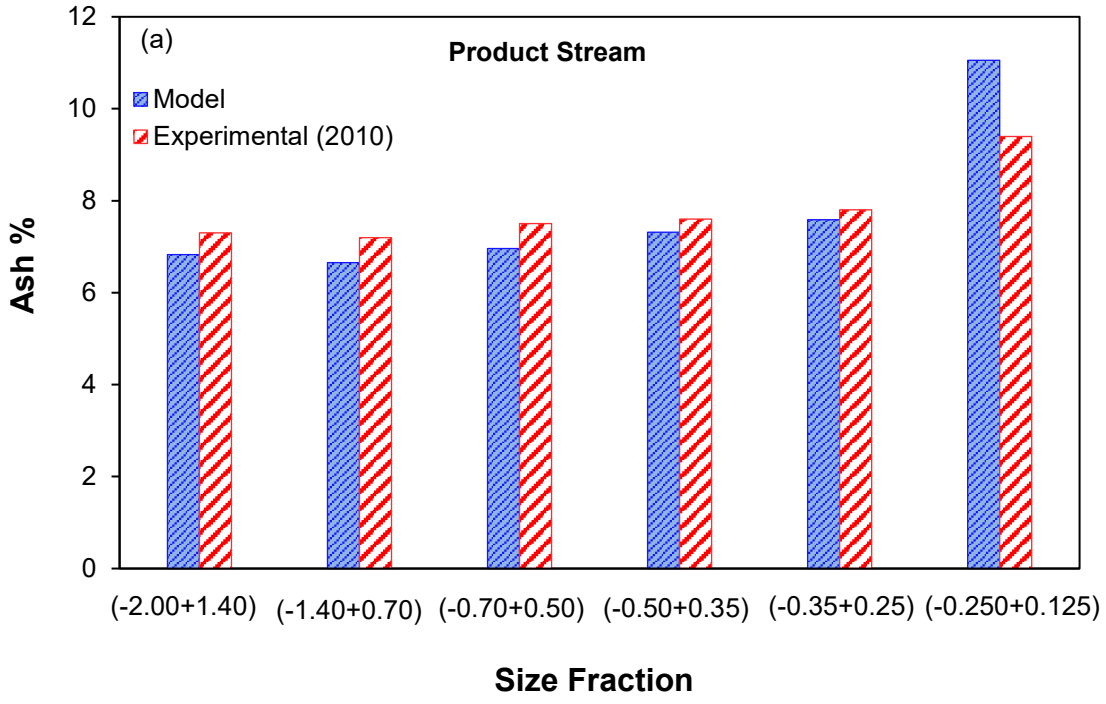

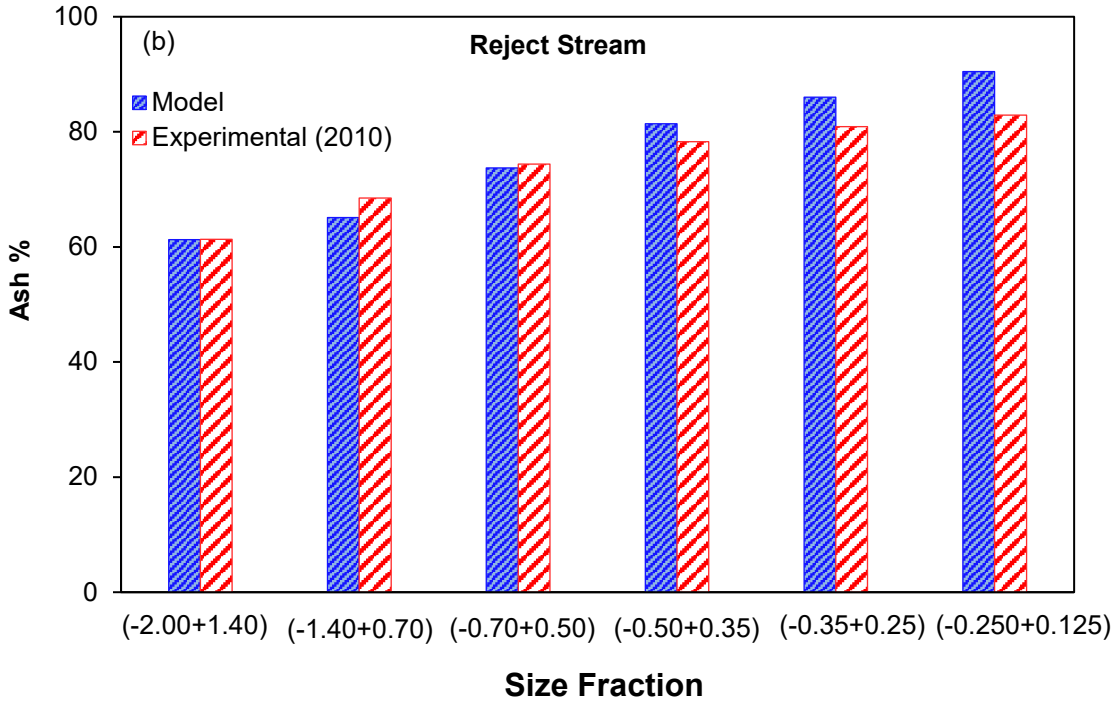

Fig. 9. Comparison of ash % in the feed and reject streams obtained through the analysis of the model predictions and the experimental results of Galvin et al. (2010): (a) Product stream; (b) Reject stream.

4.2 Volume fraction and bed profiles

Fig. 10 shows the concentration profile in the RC predicted by the segregation-dispersion model through simulations, for element numbers 1, 6 and 11. Element number 1 is the closest to the left hand side (the inclined channel is tilted towards the left), element number 6 is the middle element and element number 11 is the closest to the right hand side of the RC.

Fig. 10 shows that below the feed point the solid volume fraction increases sharply until reaching a value of 0.62, which is roughly constant between the bottom of the unit and the feed point. No significant differences were observed for the elements in the fluidization section of the RC. Furthermore, above the feed point and below the inclined channel the solid volume fraction decreased with respect to the region below the feed point. Interestingly, large differences can be observed in the inclined region. There is a low volume fraction of 0.1 formed on the left hand side of the inclined channel (element number 1). However, the solids concentration increases to a

maximum value at the middle of the channel (element number 6) due to the influence of the shear induced lift force. This force acts through the effects of the shear rate, dispersing the low density material from the sediment towards the middle of the inclined section where the transport velocities are the greatest. Thus, relatively coarse coal of lower density is efficiently transported to the overflow.

The high concentration of solids (i.e. 0.62) in the fluidization section of the RC below the feed point and especially at the bottom of the unit is due to the downwards movement of dense particles towards the discharge end (Fig. 10a-c). It is important to note that the solid concentration is the consequence of the interplay between fluidization, underflow and feed rate. Therefore, the concentration of solids can be decreased by using a higher fluidization velocity. A higher fluidization velocity produces a reduction in the suspension density, which can reverse the effects of phase inversion causing lower density coarse particles to segregate in the downwards direction, resulting in a decrease in the separation efficiency.

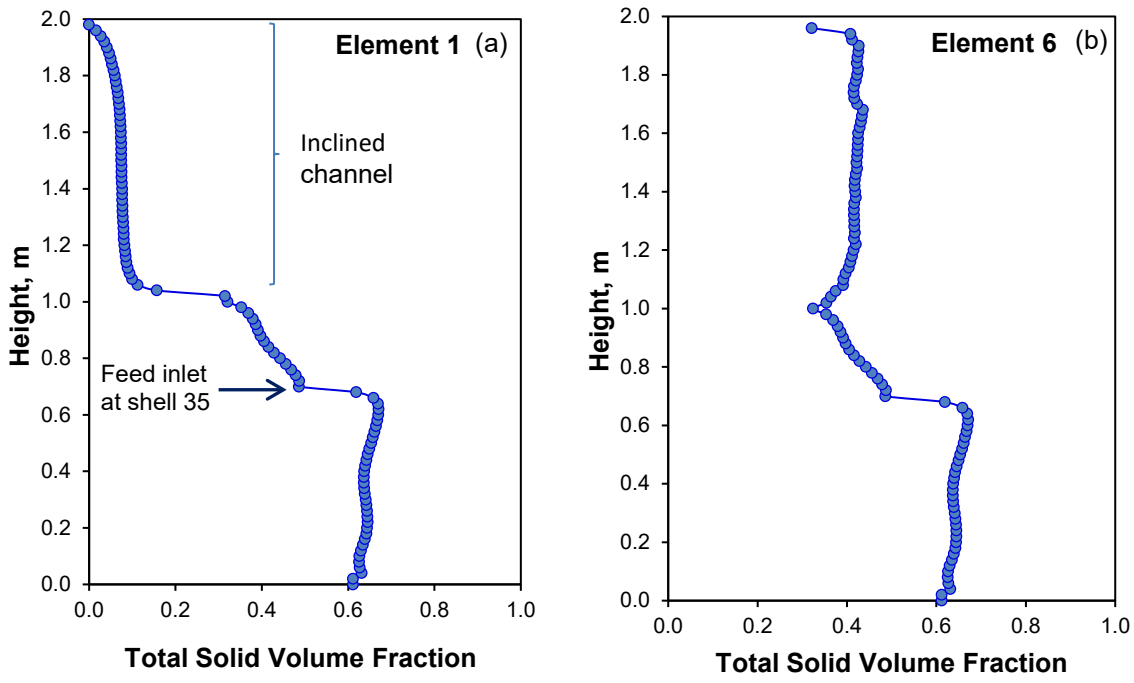

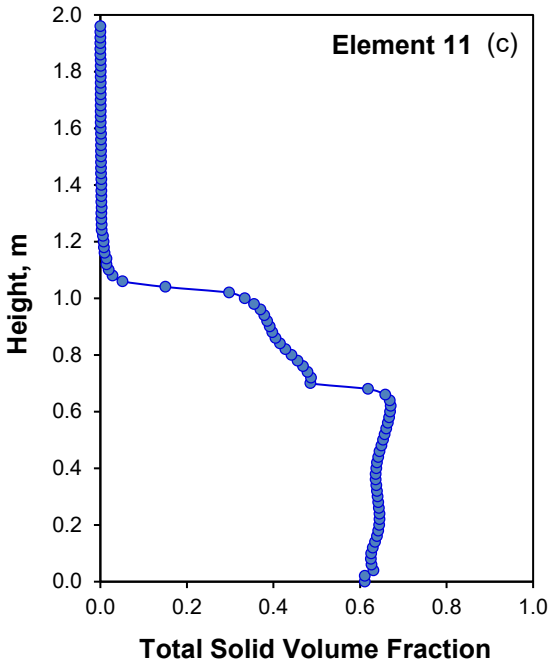

Fig. 10. Total solid volume fraction predicted by the model through simulations have been plotted as a function of column height: (a) element 1; (b) element 6; (c) element 11.

Fig. 11 shows that the total solid volume fraction increases with time across the channel width (in the x direction) at the height of 1.70 m (shell 70). The solid volume fraction reached a maximum value of 0.45 in the middle zone of the channel with time due to the mechanism of laminar shear induced lift. In contrast, the solid fraction reached a value of about 0.10 near the upward facing wall and was zero in the upper zone of the inclined channel (i.e. element 7-11).

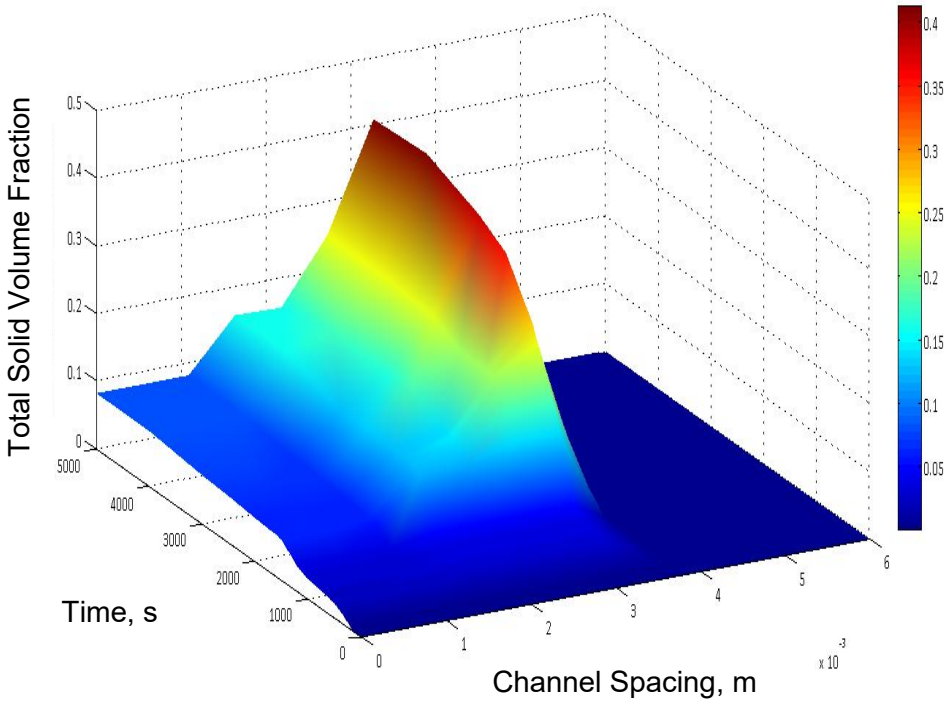

Fig. 11. 3D plot of the total solid volume fraction across the channel width in the RC at a height of 1.70 m (shell 70).

Fig. 12a displays the suspension density in the fluidization section of the RC. Although the volume fraction of the solids is practically constant below the feed inlet, as shown in Fig. 10, the actual suspension density tends to increase towards the bottom and reaches its maximum at the base of the system where a higher concentration of the heavier species is shown. On the other hand, the value of the suspension density above the feed point and below the inclined channel, i.e. between 0.7 m to 1.0 m in height, is reasonably constant.

Fig. 12b, shows the suspension density across the channel width at a height of 1.70 m (shell 70). The suspension density increased from a relatively low value of 1069 kg/m^3 to a relatively high value of 1229 kg/m^3 in the middle zone of the channel, showing the presence of a significant concentration in that zone. The suspension density decreased to a value of 1000 kg/m^3 in the upper zone of the inclined channel corresponding to the water in that zone.

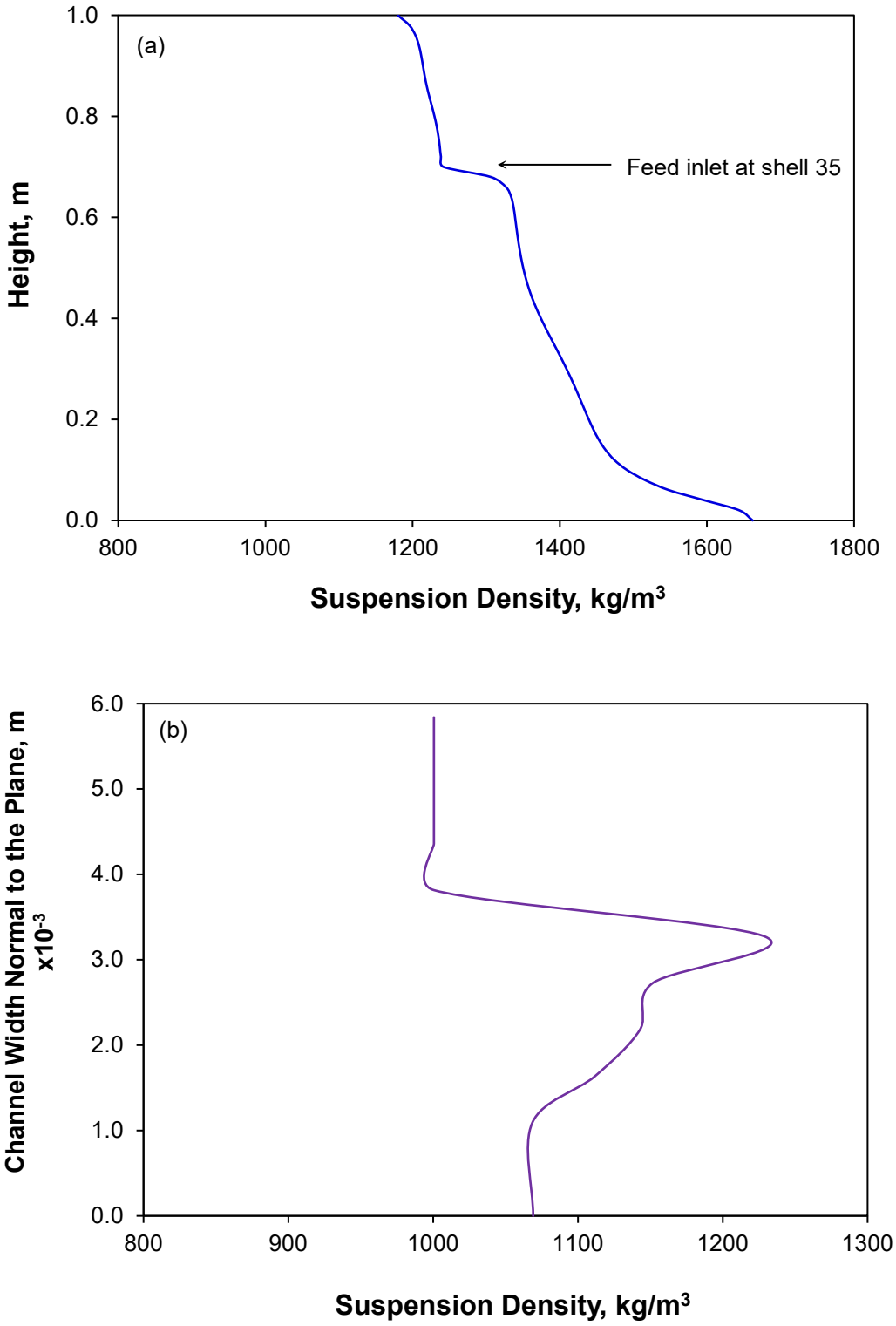

Fig. 12. Suspension density versus height predicted by the model through simulations: (a) Suspension density in the fluidization section of the RC; (b) Suspension density across the channel width in the RC at a height of 1.70 m (shell 70).

The individual solids volume fraction versus the relative particle density for each particle size at different elevations in the fluidization section is shown in Fig. 13. The data have been plotted for heights below the feed point at 0.10 m (Fig. 13a), 0.24 m (Fig. 13b), 0.40 m (Fig. 13c) and 0.60 m (Fig. 13d). Each curve shows a peak at a particular relative density which represents the particle species with the highest concentration in the system and corresponds closely to the actual value of D_{50} of the respective particle size range. The peaks also infer that the bed in the fluidization section was mainly composed of particle species representing the D_{50} for their respective particle size ranges, given these particles have an equal chance of reporting to the underflow and overflow.

For some particle size ranges in the simulation, the actual separation density, i.e. D_{50}, does not correspond to any physical size used in the simulations, so the particle species having a density closer to the D_{50} are the ones that show higher concentration (Fig. 13). For instance, the D_{50} for particle size 1.70 mm is 1.54, (Fig. 6), but in the simulations, particles with relative density 1.45 and 1.60 were considered (Table 1). Therefore, particle species with relative density 1.45 and 1.60 display higher concentration at different elevations in the fluidization section of the RC. Similarly, for a particle size of 0.30 mm, a more homogenous concentration of particles with relative density 1.80 against the actual value of the D_{50} of 1.82, has been observed.

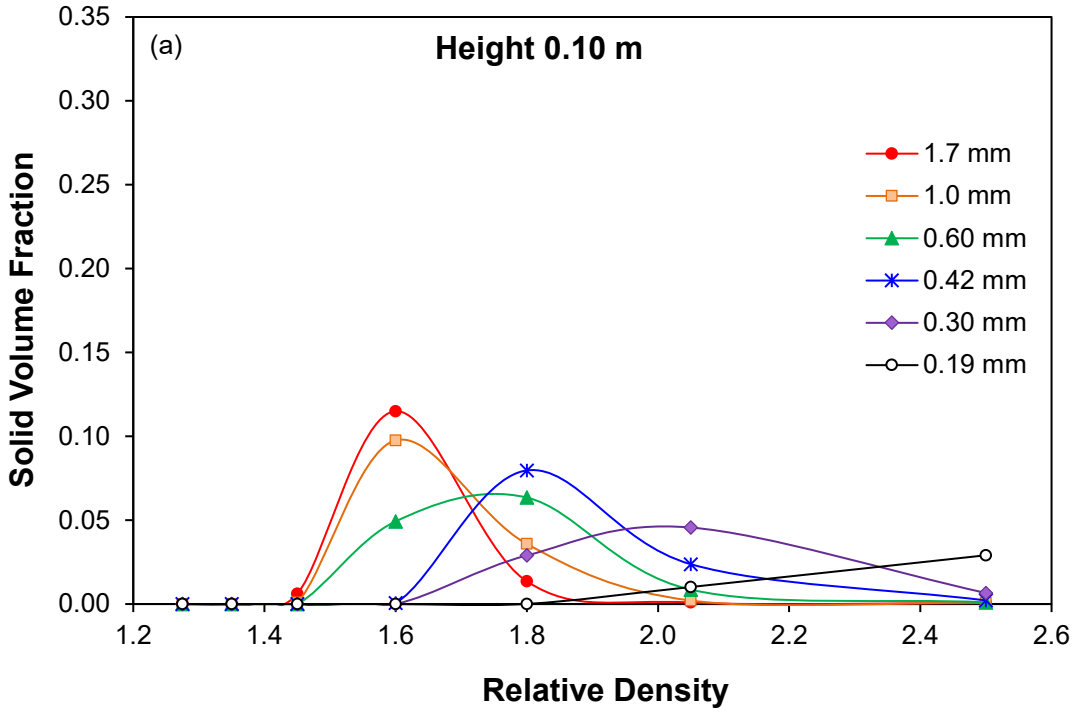
(a)
Height 0.10 m
Solid Volume Fraction
Relative Density
0.35
0.30
0.25
0.20
0.15
0.10
0.05
0.00
1.2
1.4
1.6
1.8
2.0
2.2
2.4
2.6
1.7 mm
1.0 mm
0.60 mm
0.42 mm
0.30 mm
0.19 mm

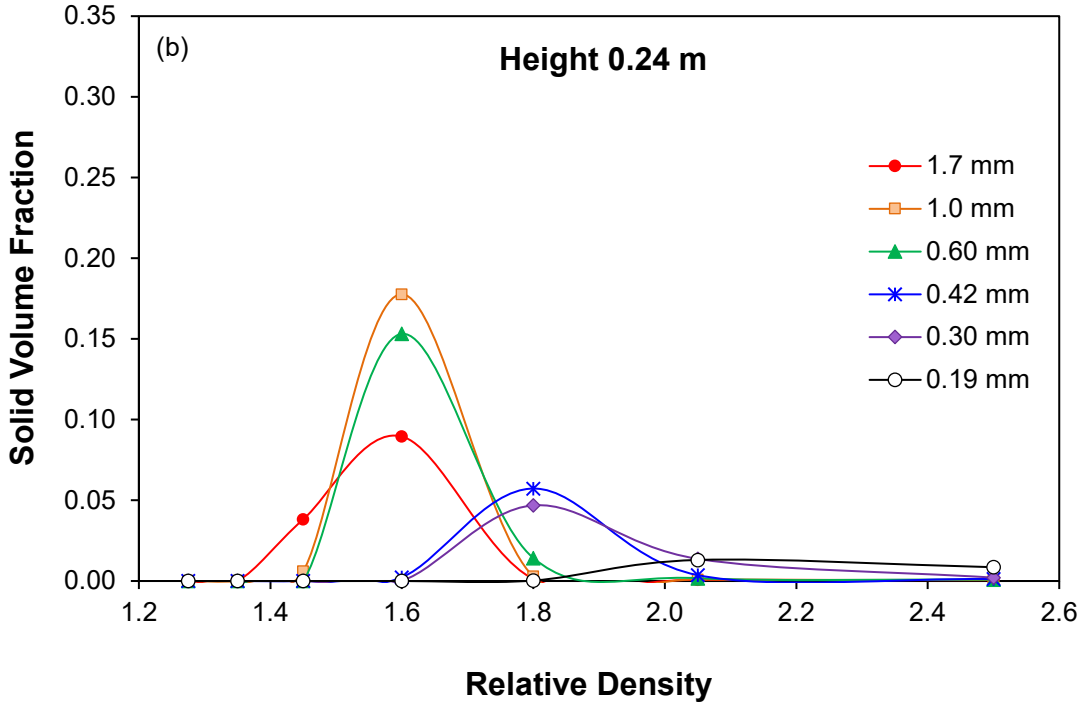
(b)
Height 0.24 m
Solid Volume Fraction
Relative Density
0.35
0.30
0.25
0.20
0.15
0.10
0.05
0.00
1.2
1.4
1.6
1.8
2.0
2.2
2.4
2.6
1.7 mm
1.0 mm
0.60 mm
0.42 mm
0.30 mm
0.19 mm

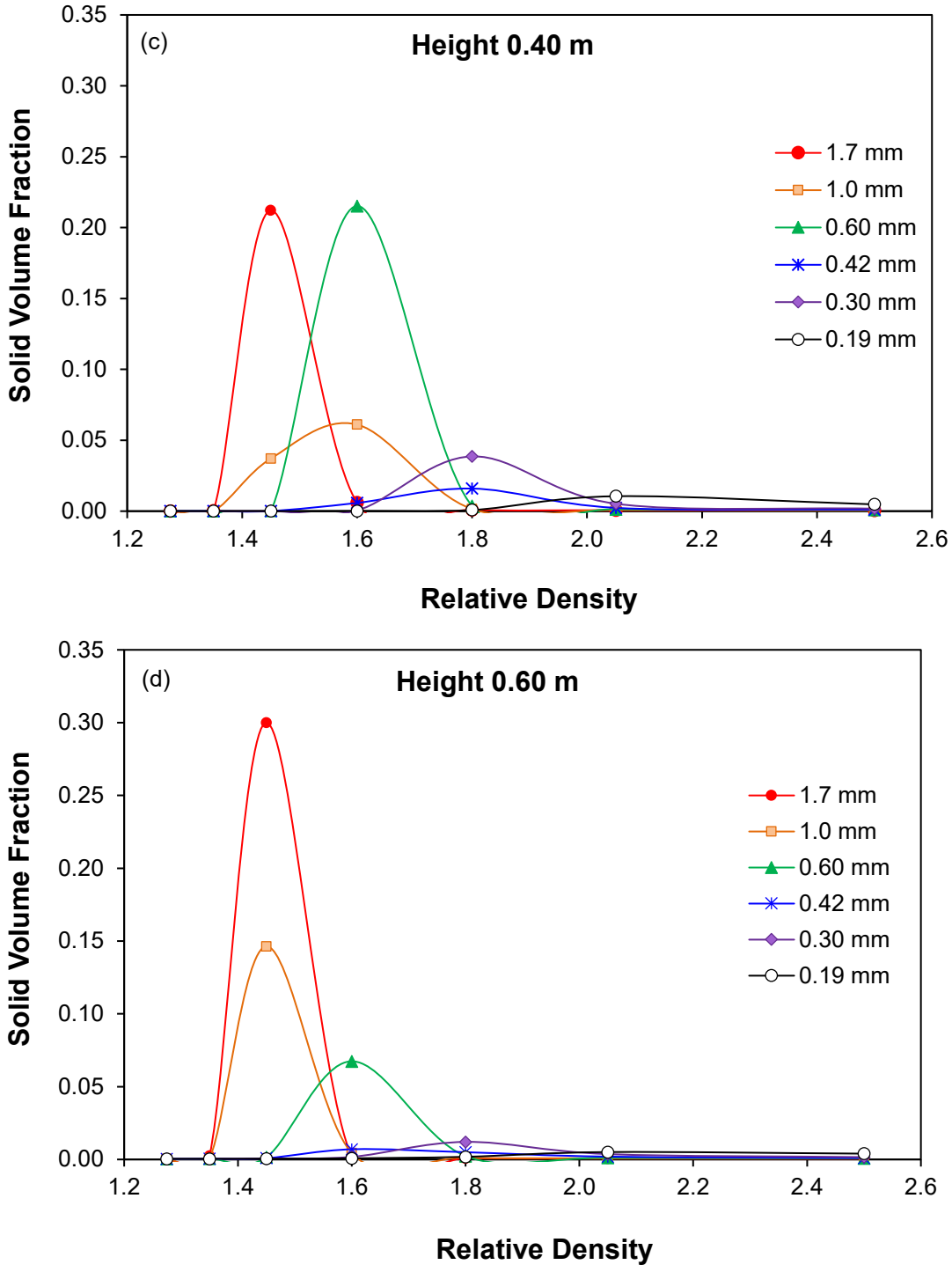

Fig. 13. Individual solid volume fraction versus Relative density at different levels within the fluidization section of the RC from the model: (a) volume fraction versus relative density at a height 0.10 m; (b) volume fraction versus relative density at a height 0.24 m; (c) volume fraction versus relative density at a height 0.40 m; (d) volume fraction vs relative density at a height 0.60 m.

To better illustrate the values at which peaks in Fig. 13 are observed, the relative density of particle species close to the actual D_{50} values of corresponding particle sizes are tabulated in Table 2.

Table 2: Particle species showing peaks at different elevations in the fluidization section of the RC, having relative density close to the actual D_{50} of a particular particle size.

Particle sizes (mm)	D_{50}	Relative density of particles with highest concentrations			
		Elevation 0.1 m	Elevation 0.24 m	Elevation 0.40 m	Elevation 0.60 m
0.19	**2.22**	2.50 2.05	2.50 2.05	2.05	2.05
0.30	**1.82**	1.80 2.05	1.80	1.80	1.80
0.42	**1.70**	1.80	1.80	1.80	1.60
0.60	**1.62**	1.60 1.80	1.60 1.80	1.60	1.60
1.0	**1.57**	1.60	1.60	1.60 1.45	1.45
1.7	**1.54**	1.60	1.60 1.45	1.45	1.45

5. Effect of high solids throughputs on separation performance

The segregation-dispersion model was also used to investigate the effect of high solids throughputs on separation performance in the RC, according to the runs reported by Galvin et al. (2010). The fluidization rate was kept constant as mentioned in section 3, for the solids throughputs of 6.3 t/m^{2}h and 9.8 t/m^{2}h according to Galvin et al. (2010). While, the fluidization velocities in the simulations were kept at 7.0 m^3/m^{2}h (0.0020 m^3/m^{2}s) and 7.5 m^3/m^{2}h (0.0021 m^3/m^{2}s) for the solids throughputs of 21.3 t/m^{2}h (0.0035 m^3/m^{2}s) and 47.3 t/m^{2}h (0.0080 m^3/m^{2}s), respectively, consistent with that used experimentally by Galvin et al. (2010). Fig. 14 demonstrates the effect of increasing throughput on the D_{50} values versus particle size. It was observed that there was not much difference in the values of the D_{50} for coarser particles at the higher throughputs, and that the system continued to perform. However, the difference in values of the D_{50} of the fine particles over the range of throughputs used was significant. This is because high throughputs tend to cause the finer particles to report to the system overflow.

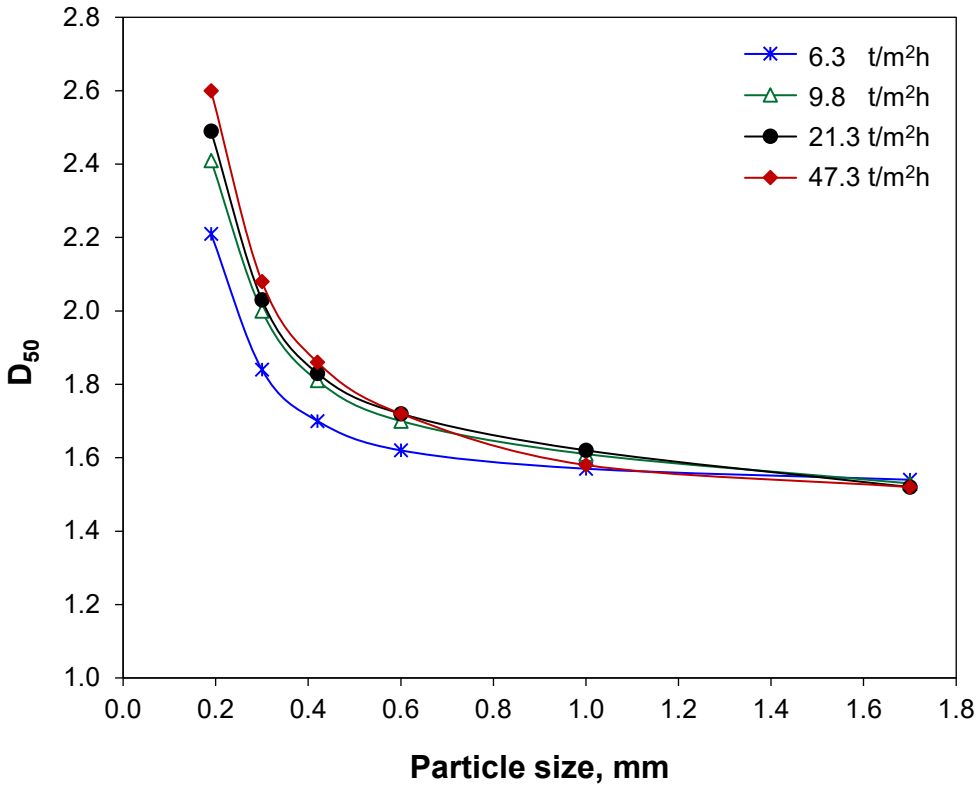

Fig. 14. The separation relative density, D_{50}, obtained through simulations, have been shown as a function of particle size at different solids throughputs of 6.3 t/m^{2}h (0.0011 m^3/m^{2}s), 9.8 t/m^{2}h (0.0016 m^3/m^{2}s), 21.3 t/m^{2}h (0.0035 m^3/m^{2}s) and 47.3 t/m^{2}h (0.0080 m^3/m^{2}s).

Similarly, Fig. 15 shows the effect of different solid throughputs on the Ep values as a function of particle size. A monotonic decrease in the Ep values with increase in particle size can be observed for all solid throughputs. The results show that for the coarser particles, the values of Ep remains very low, i.e. less than 0.05, even at higher throughputs, thus proving sharp separation. In contrast, at 21.3 t/m^{2}h and 47.3 t/m^{2}h solids throughputs, a sharp increase in the Ep values for fine particles species has been observed. This observation further strengthens the fact that at high solid throughputs the separation of fine particles is poor, and particles tend to report to the overflow. This is because at high solids throughputs, fine particle species were conveyed from the system at a relatively high rate due to the relatively high value of the hydraulic velocity in the channel. Therefore, the separation of the finer particle species was poorer and hence a higher Ep value was observed.

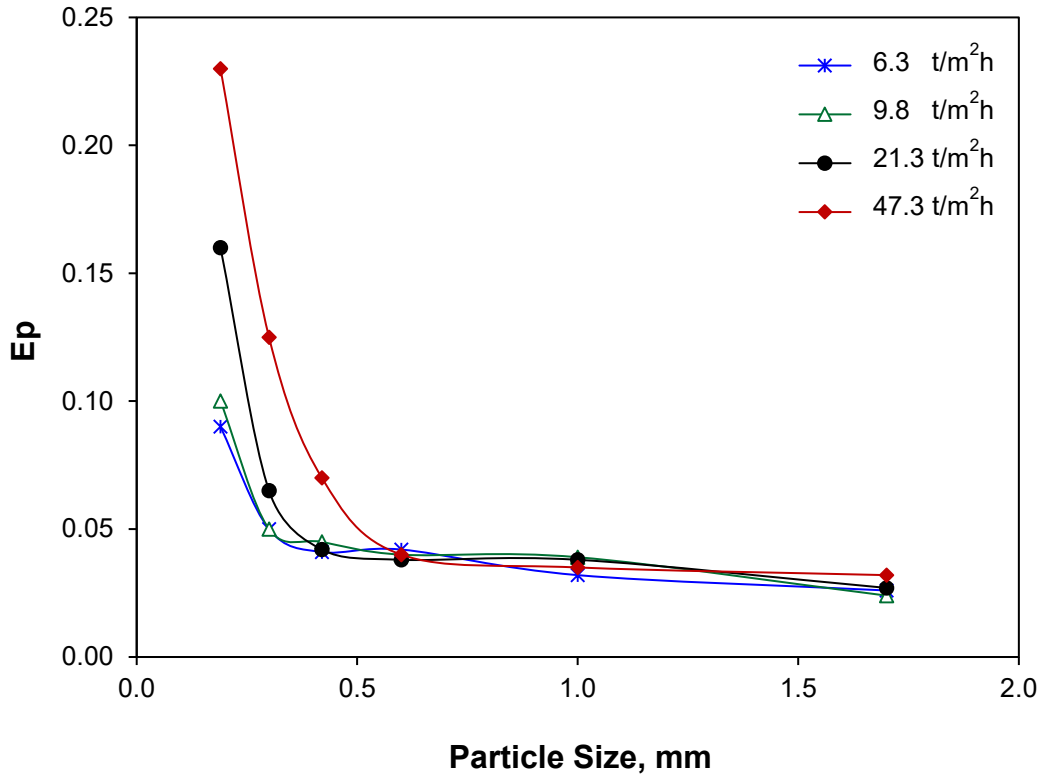

Fig. 15. The Ecart probable error, Ep, obtained through simulations, have been shown as a function of particle size at different solid throughputs of 6.3 t/m^{2}h (0.0011 m^3/m^{2}s), 9.8 t/m^{2}h (0.0016 m^3/m^{2}s), 21.3 t/m^{2}h (0.0035 m^3/m^{2}s) and 47.3 t/m^{2}h (0.0080 m^3/m^{2}s).

The partition curves for high solid throughputs are not available for the experimental results of Galvin et al. (2010). However, the authors (Galvin et al., 2010) have provided the analysis of experimental runs to show the fractional and cumulative ash % of the feed, product and reject streams, shown in Table A3. In order to validate the model predictions for higher solid throughputs, an analysis of simulation data has been done to show the fractional and cumulative ash % of the product and reject stream and is listed in Table A4. A comparison between the model predictions and the experimental results have been shown in the form of bar charts in Figures 16 and 17.

Fig. 16 represents a comparison of model prediction and experimental results of Galvin et al. (2010) of mass fraction for a solid throughput of 21.3 t/m^{2}h. The values of mass fraction obtained by simulations closely match with the experimental results, thus proving the impact of the model in handling higher throughputs and to predict results close to real systems.

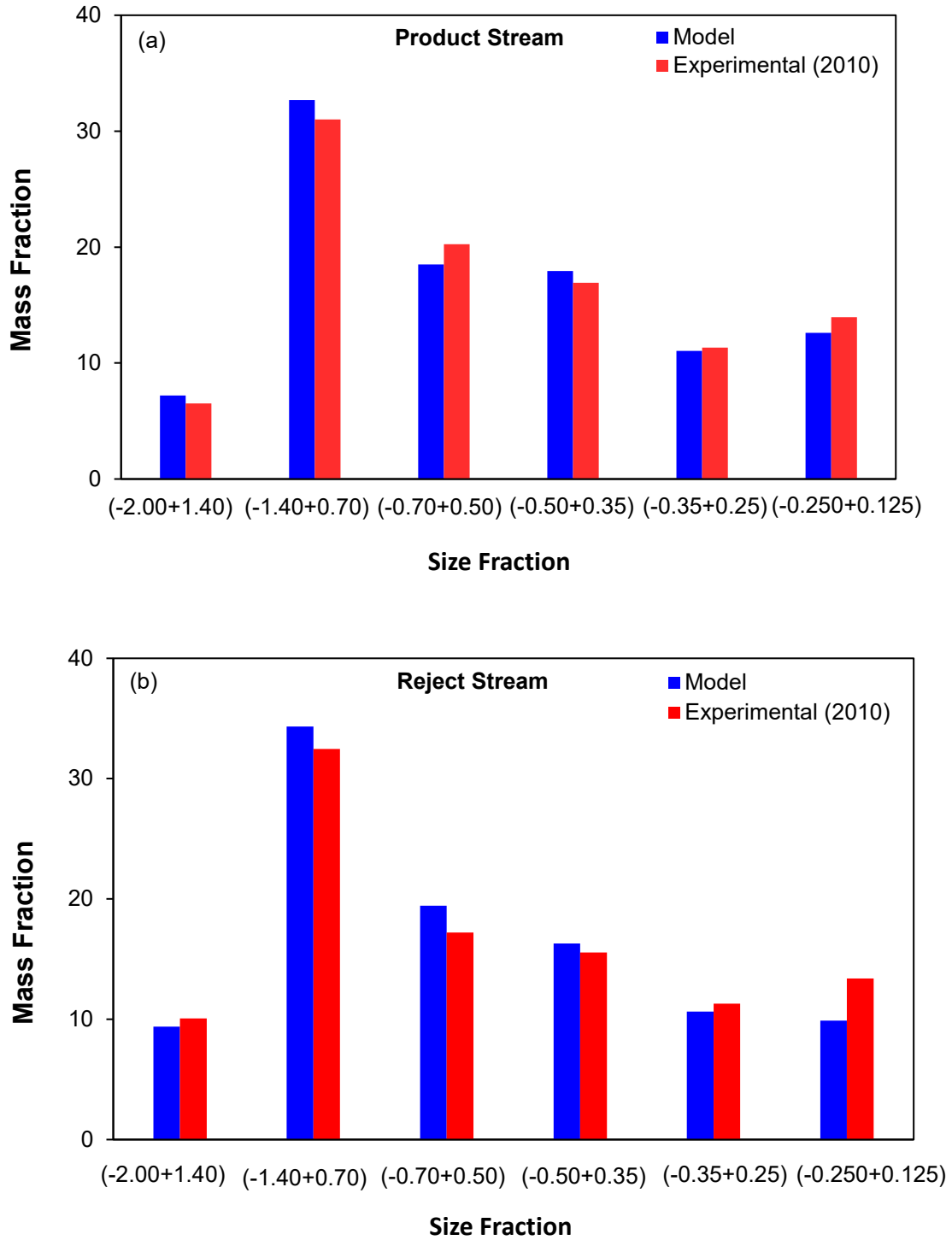

Fig. 16. Comparison of mass fraction in the feed and reject streams obtained through the analysis of model predictions and the experimental results of Galvin et al. (2010). The results are taken for the solid throughput of 21.3 t/m^{2}h: (a) Product stream; (b) Reject stream.

Fig. 17 represents a comparison of model prediction and experimental results of Galvin et al. (2010) of ash % for a solid throughput of 21.3 t/m^{2}h. The values of ash % obtained by simulations closely match with the experimental results. The main discrepancy is observed again for the fine particle of size fraction -0.250+0.125 mm, which indicates that large amount of fines report to overflow at high solid throughput.

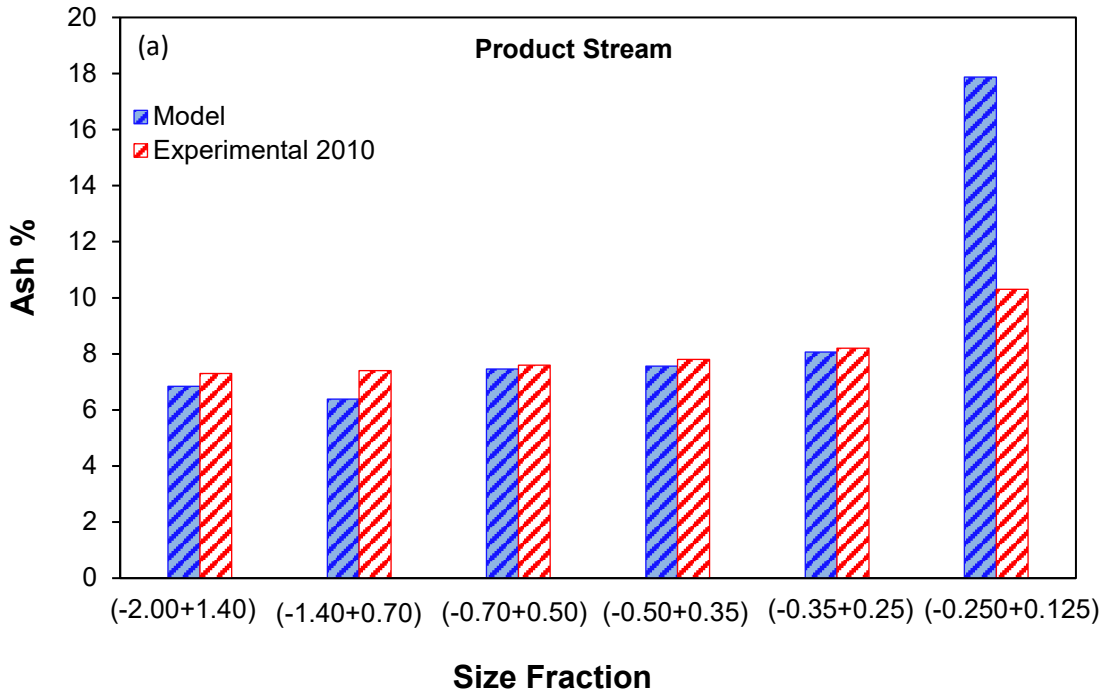

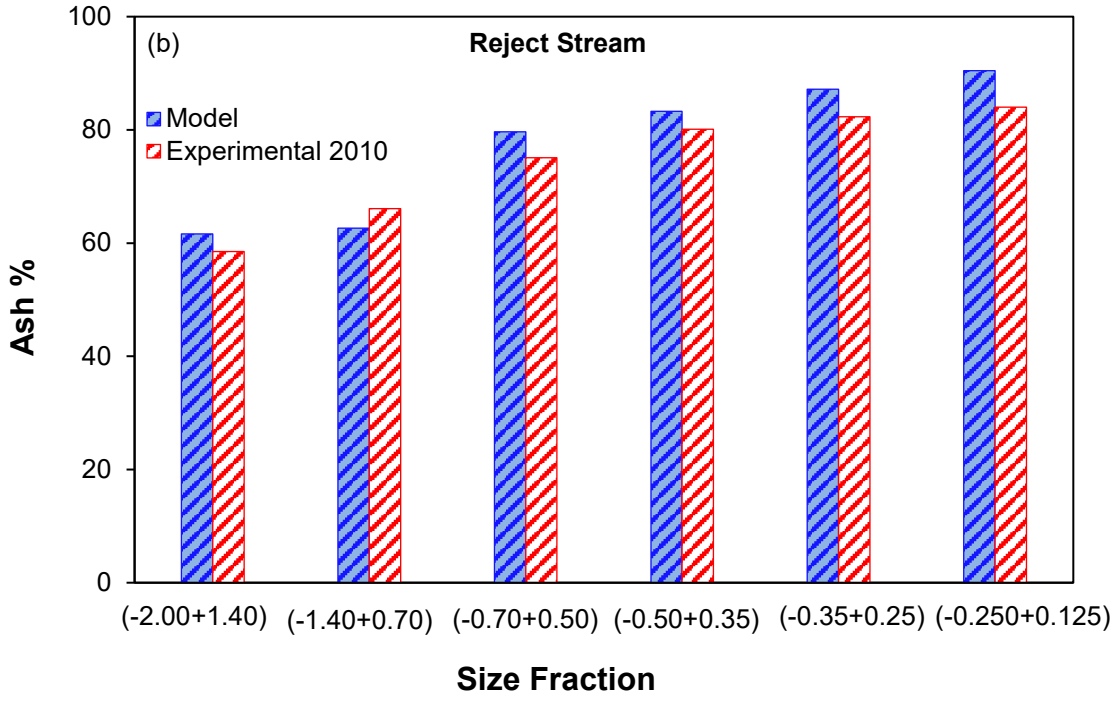

Fig. 17. Comparison of ash % in the feed and reject streams obtained through the analysis of model predictions and the experimental results of Galvin et al. (2010). The results are taken for the solid throughput of 21.3 t/m^{2}h: (a) Product stream; (b) Reject stream.

Overall, the model predictions for higher solid throughputs gave a very good agreement with the experimental results of Galvin et al. (2010). Therefore, the partition curves obtained through simulations using the segregation-dispersion model of the RC for higher solid throughputs can be considered as a representation of the real system. Figure B1 in Appendix-B shows partition curves for the solid throughputs of 21.3 t/m^{2}h and 47.3 t/m^{2}h, obtained through simulations.

6. Conclusions

A computational approach has been used to simulate the Reflux Classifier (RC) using a segregation-dispersion model for the first time. The model has been developed to investigate the separation of multicomponent species, having different densities and sizes, under continuous process conditions. The model, which incorporates hindered settling and shear-induced hydrodynamic dispersion, is simple and robust, and

capable of describing the complexity of multiple species undergoing segregation and dispersion during their transport within the RC.

The results of the segregation-dispersion model were in reasonably good agreement with the experimental results of Galvin et al. (2010) for particle species in the size range -2.0 +0.25 mm, in terms of the variation in the D_{50} and Ep values with particle size. The model showed that the D_{50} and Ep decreased monotonically with size, similar to the experimental observations. However, some discrepancies existed in the values of these parameters for the fine particle species of size -0.250 +0.125 mm. The D_{50} predicted by the model for the fine fraction was larger than the value obtained experimentally. A similar trend was observed for the Ep results, with a break-away effect evident below 0.250 mm.

It is possible that the nonconformity of the simulations and the experimental results could be due to deficiencies in the continuum model in dealing with fine particles in the inclined channel. The detailed physics associated with the interactions of the particles at the inclined surface are complex. For example, the influence of the sliding sediment on the fluid velocity profile inside the inclined channel has been neglected here. Further work is required to properly investigate the separation of the relatively fine particles. It is further noted that in practice the simulated break-away effect can be observed, so the discrepancy could also be associated with the experimental data.

The simulation model also provides an improved understanding of the internal distribution of the particle species at steady state. While the suspension density increased towards the bottom of the unit due to an increase in the presence of denser components, the solid volume fraction remained nearly constant. In contrast, above the feed point the solid volume fraction decreased with height while the suspension density became constant. The results also show that, the bed in the vertical section of the RC unit, mostly comprised of particle species whose densities were close to the D_{50}.

The effect of increasing throughputs on the separation performance was also investigated through simulations using the segregation-dispersion model for the RC.

Comparisons of analysis of experimental results of Galvin et al. (2010) and model predictions for the fractional and cumulative ash % of feed, product and reject streams are provided, which showed good agreement between experimental results and model predictions.

Acknowledgements

The authors acknowledge the support of the University of Newcastle, in granting N.H.Syed a scholarship. The authors also acknowledge the financial support of the Australian Research Council (ARC) (LP140100325), and the Australian Coal Association Research Program (ACARP), and FLSmidth.

Appendix-A – Analysis of feed, product and reject streams

An analysis of the simulations data obtained by using continuum segregation-dispersion model of the RC has been carried out to show the fractional and cumulative ash % for narrow size fraction of the feed, product and reject streams. The simulation results are tabulated in Table A1 and experimental results of Galvin et al. (2010) are listed in Table A2 for the solid throughput of 6.3 t/m^{2}h. Similarly, the experimental results of Galvin et al. (2010) and simulation results of solid throughput 21.3 t/m^{2}h are listed in Tables A3 and A4 respectively. A comparison of the fractional and cumulative ash % of the product and reject streams of the experimental work of Galvin et al. (2010) and model predictions gave a very good agreement.

The tables show feed conditions for the particle size range -2.00+0.125 mm, because the size fractions +2.00, -0.125+0.075, -0.075+0.0 were neglected during the simulations. The particle size range -2.00+0.125 mm was selected, keeping in view the computational limitations and also the size range in which the feed mostly consisted of high mass fraction.

Table A1: Analysis of the model results obtained through simulations, showing the fractional and cumulative ash % for narrow size fraction of the feed, product and reject streams. The results have been tabulated for the solid throughput of 6.3 t/m^{2}h, for the particle size range -2.00+0.125 mm.

Size fraction	Feed Stream				Product Stream				Reject Stream			
	Fractional		Cumulative		Fractional		Cumulative		Fractional		Cumulative	
	Mass	Ash	Mass	Ash	Mass	Ash	Mass	Ash	Mass	Ash	Mass	Ash
-2.00+1.40	7.5	17.9	7.5	17.9	7.3	6.8	7.3	6.8	8.6	61.3	8.6	61.3
-1.40+0.70	34.0	16.2	41.5	16.5	33.6	6.7	40.9	6.7	30.0	65.1	38.6	64.2
-0.70+0.50	16.8	18.8	58.2	17.2	18.3	7.0	59.1	6.8	20.4	73.7	59.0	67.5
-0.50+0.35	17.0	17.2	75.2	17.2	18.0	7.3	77.2	6.9	15.8	81.4	74.8	70.5
-0.35+0.25	11.7	19.0	86.9	17.4	11.1	7.6	88.3	7.0	10.7	86.0	85.5	72.4
-0.250+0.125	13.1	24.3	100.0	18.3	11.7	11.1	100.0	7.5	14.4	90.5	100.0	75.0

Table A2: Analysis of the experimental results provided in Table B3 by Galvin et al. (2010), showing the fractional and cumulative ash % for narrow size fraction of the feed, product and reject streams. The results have been tabulated for the solid throughput of 6.3 t/m^{2}h, for the particle size range -2.00+0.125 mm.

Size fraction	Feed Stream				Product Stream				Reject Stream			
	Fractional		Cumulative		Fractional		Cumulative		Fractional		Cumulative	
	Mass	Ash	Mass	Ash	Mass	Ash	Mass	Ash	Mass	Ash	Mass	Ash
-2.00+1.40	7.5	17.9	7.5	17.9	7.1	7.3	7.1	7.3	9.3	62.4	9.3	62.4
-1.40+0.70	34.0	16.2	41.5	16.5	34.2	7.2	41.2	7.2	27.6	68.5	36.8	67.0
-0.70+0.50	16.8	18.8	58.2	17.2	17.8	7.5	59.0	7.3	19.7	74.4	56.5	69.6
-0.50+0.35	17.0	17.2	75.2	17.2	18.5	7.6	77.5	7.4	15.9	78.3	72.4	71.5
-0.35+0.25	11.7	19.0	86.9	17.4	11.4	7.8	88.9	7.4	11.0	80.9	83.4	72.7
-0.250+0.125	13.1	24.3	100.0	18.3	11.1	9.4	100.0	7.6	16.6	82.9	100.0	74.4

Table A3: Analysis of the experimental results provided in Table B5 by Galvin et al. (2010), showing the fractional and cumulative ash % for narrow size fraction of the feed, product and reject streams. The results have been tabulated for the solid throughput of 21.3 t/m^{2}h, for the particle size range -2.00+0.125 mm.

Size fraction	Feed Stream				Product Stream				Reject Stream			
	Fractional		Cumulative		Fractional		Cumulative		Fractional		Cumulative	
	Mass	Ash	Mass	Ash	Mass	Ash	Mass	Ash	Mass	Ash	Mass	Ash
-2.00+1.40	7.1	17.0	7.1	17.0	6.5	7.3	6.5	7.3	10.1	58.5	10.1	58.5
-1.40+0.70	31.2	15.4	38.3	15.7	31.0	7.4	37.5	7.4	32.5	66.1	42.5	64.3
-0.70+0.50	21.0	14.5	59.3	15.3	20.3	7.6	57.8	7.5	17.2	75.1	59.8	67.4
-0.50+0.35	16.3	16.7	75.6	15.6	16.9	7.8	74.7	7.5	15.6	80.1	75.3	70.0
-0.35+0.25	10.4	18.9	86.1	16.0	11.3	8.2	86.0	7.6	11.3	82.3	86.6	71.6
-0.250+0.125	13.9	22.6	100.0	16.9	14.0	10.3	100.0	8.0	13.4	84.0	100.0	73.3

Table A4: Analysis of the model results obtained through simulations, showing the fractional and cumulative ash % for narrow size fraction of the feed, product and reject streams. The results have been tabulated for the solid throughput of 21.3 t/m^{2}h, for the particle size range -2.00+0.125 mm.

Size fraction	Feed Stream				Product Stream				Reject Stream			
	Fractional		Cumulative		Fractional		Cumulative		Fractional		Cumulative	
	Mass	Ash	Mass	Ash	Mass	Ash	Mass	Ash	Mass	Ash	Mass	Ash
-2.00+1.40	7.1	17.0	7.1	17.0	7.2	6.8	7.2	6.8	9.4	61.6	9.4	61.6
-1.40+0.70	31.2	15.4	38.3	15.7	32.7	6.4	39.9	6.5	34.3	62.7	43.7	62.4
-0.70+0.50	21.0	14.5	59.3	15.3	18.5	7.5	58.4	6.8	19.4	79.6	63.2	67.7
-0.50+0.35	16.3	16.7	75.6	15.6	17.9	7.6	76.3	7.0	16.3	83.3	79.5	70.9
-0.35+0.25	10.4	18.9	86.1	16.0	11.0	8.1	87.4	7.1	10.6	87.2	90.1	72.8
-0.250+0.125	13.9	22.6	100.0	16.9	12.6	17.9	100.0	8.5	9.9	90.4	100.0	74.6

Tables A5, and A6 are provided to show the washability data of the feed. Table A5 shows the washability data of the original feed used during the experimental runs by Galvin et al. (2010), with the mass portions totalling 1000 units. A three-step process was used to form the final data set used in the simulations. In Tables A6 the number of size fractions was reduced and certain density ranges were combined to reduce the number of density fractions in order to focus on the species to be modelled. The mass portion of the size fraction -4.00+2.00 was added in -2.00+1.40 while the size fraction -0.125+0.0 was neglected as being very fine particle species. Similarly, certain density ranges like 1.55 and 1.65, 1.75 and 1.85, 1.95 and 2.10, and 2.30, 2.50, 2.70 were combined to give average densities 1.60, 1.80, 2.05 and 2.50 respectively. Finally the data values were adjusted so that the mass portions added to give 1000 units.

Table A5: Washability data of the feed used in the experimental runs by Galvin et al. (2010).

Size fraction	Relative Density											
	1.27	1.35	1.45	1.55	1.65	1.75	1.85	1.95	2.10	2.30	2.50	2.70
-4.00+2.00	2.03	2.35	0.38	0.29	0.20	0.19	0.12	0.10	0.14	0.28	0.29	0.1
-2.00+1.40	27.18	20.05	6.77	1.81	1.61	1.18	0.93	0.65	1.12	2.19	3.03	0.8
-1.40+0.70	150.85	87.70	27.08	10.56	5.24	4.07	3.38	2.56	3.66	6.67	14.13	5.2
-0.70+0.50	85.68	41.81	12.53	6.87	3.97	2.27	1.84	1.55	2.61	4.19	13.08	5.4
-0.50+0.35	84.54	38.41	12.83	5.75	3.58	1.88	1.33	0.94	1.85	3.48	9.75	7.8
-0.35+0.25	52.72	23.07	6.90	3.71	2.26	1.03	0.60	0.60	1.09	2.50	6.91	6.6
-0.250+0.125	41.18	32.64	7.72	4.28	2.77	1.77	0.91	0.51	1.24	3.13	11.31	11.2
-0.125+0.0	5.63	3.39	1.68	1.16	0.83	0.68	0.52	0.40	0.54	0.62	4.15	4.9

Table A6: Washability data of the feed used in the simulations. The mass portions have been adjusted to give 1000 units.

	Relative Density						
Size fraction	1.27	1.35	1.45	1.60	1.80	2.05	2.50
-2.00+1.40	29.95	22.96	7.33	4.00	2.48	2.06	6.81
-1.40+0.70	154.64	89.90	27.76	16.20	7.64	6.38	26.67
-0.70+0.50	87.83	42.86	12.85	11.11	4.22	4.26	23.19
-0.50+0.35	86.67	39.38	13.16	9.57	3.29	2.86	21.60
-0.35+0.25	54.04	23.65	7.08	6.13	1.67	1.74	16.44
-0.250+0.125	42.21	33.46	7.91	7.22	2.75	1.79	26.28

Appendix-B – Partition curves at high solid throughputs

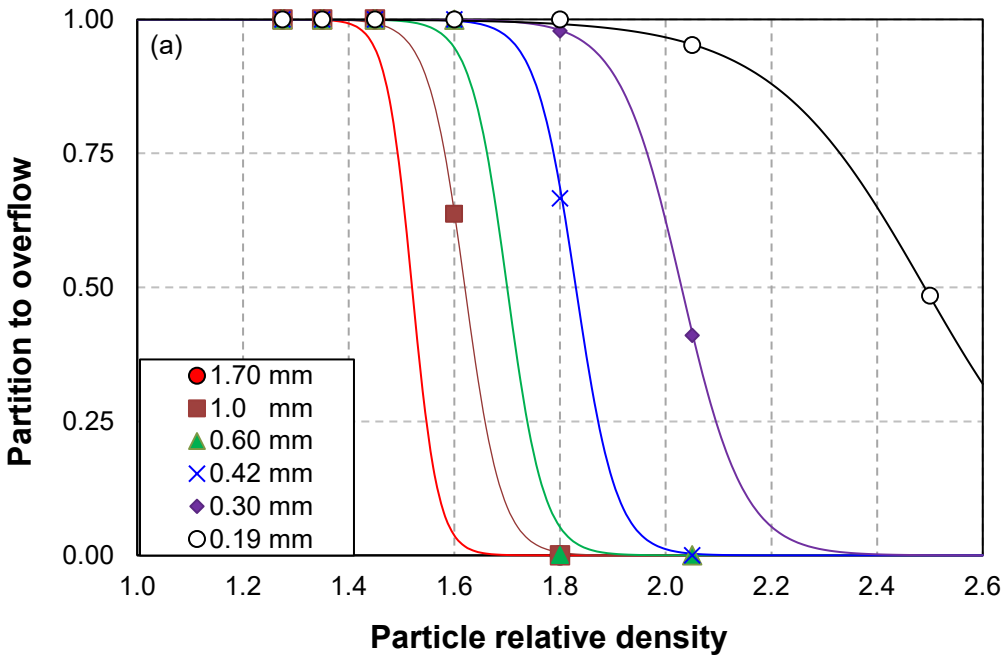

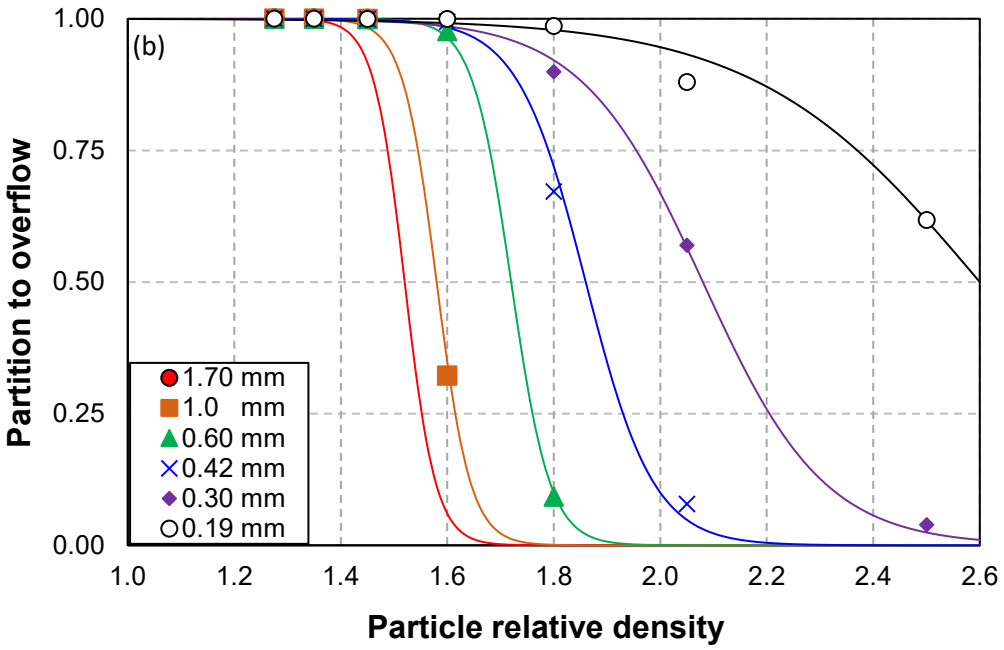

Fig. B1. Partition curves obtained through simulations for the particle size range -2.0+0.125 mm for higher solid throughputs. In the Figure, running from left to right across the graph, the curves representing narrow size fraction -2.0+1.40 mm, -1.40+0.70 mm, -0.70+0.50 mm, -0.50+0.35 mm, -0.35+0.25 mm and -0.250+0.125 mm respectively; (a) 21.3 t/m^{2}h; (b) 47.3 t/m^{2}h.

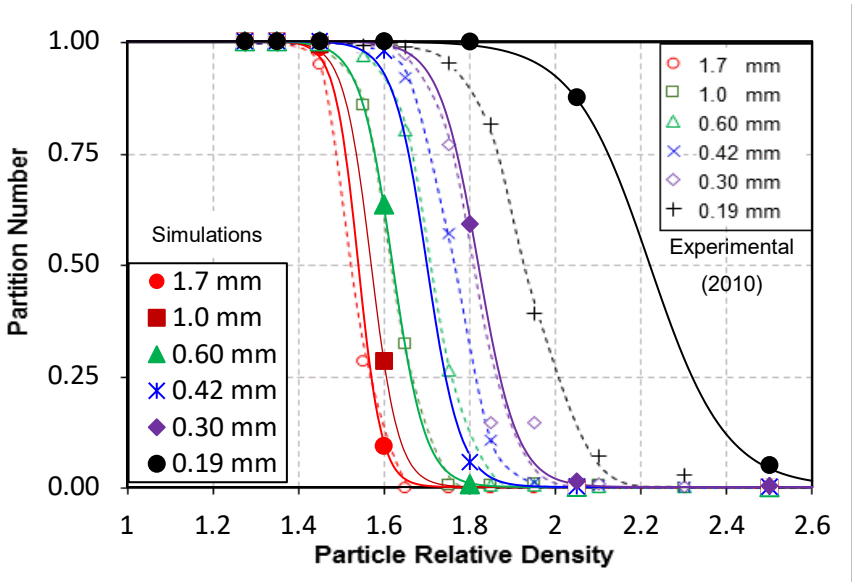

Fig. B2. Combined individual partition curves obtained from the experimental results and the model predictions. The dashed lines represent the experimental results and the continuous lines represent the model predictions.

References

Amariei, D., Michaud, D., Paquet, G., Lindsay, M., 2014. The use of a Reflux Classifier for iron ores: Assessment of fine particles recovery at pilot scale. Mineral Engineering 62, 66 – 73.

Asif, M., 1997. Modelling of multi-solid liquid fluidized beds. Chemical Engineering Technology 20, 485–490.

Asif, M., 1998. Segregation velocity model for fluidized suspension of binary mixture of particles. Chemical Engineering and Processing 37, 279 – 286.

Asif, M., 2004. The complete segregation model for a liquid fluidized bed: formulation and related issues. Powder Technology 140, 21 – 29.

Asif, M., Petersen, J.N., 1993. Particle dispersion in a binary solid–liquid fluidized bed. A.I.Ch.E. Journal 39 (9), 1465 – 1471.

Boycott, A.E., 1920. Sedimentation of blood corpuscles. Nature 104, 532.

Callen, A., Moghtaderi, B., Galvin, K.P., 2007. Use of parallel inclined plates to control elutriation from a gas fluidized bed. Chemical Engineering Science 62, 356 – 370.

Chen, A., Grace, J.R., Epstein, N., Lim C. J., 2002. Steady state dispersion of mono-size, binary and multi-size particles in a liquid fluidized bed classifier. Chemical Engineering Science 57, 991 – 1002.

Cornelissen, J.T., Taghipour, F., Escudie, R., Ellis, N., Grace, J.R., 2007. CFD modelling of a liquid-solid fluidized bed. Chemical Engineering Science 62, 6334 – 6348.

Di Felice, R., 1995. Hydrodynamics of liquid fluidization. Chemical Engineering Science 50, 1213–1245.

Di Felice, R., 2007. Liquid suspensions of single and binary component solid particles-An overview. China Particulogoy 5, 312-320.

Dickinson, J.E., Galvin, K.P., 2014. Fluidized bed desliming in fine particle flotation – part 1. Chemical Engineering Science 108, 283 – 298.

Doroodchi, E., Fletcher, D.F., Galvin, K.P., 2004. Influence of inclined plates on the expansion behaviour of particulate suspensions in a liquid fluidized bed. Chemical Engineering Science 59, 3559 – 3567.

Doroodchi, E., Zhou, J., Fletcher, D.F., Galvin, K.P., 2006. Particle size classification in a fluidized bed containing parallel inclined plates. Minerals Engineering 19, 162 – 171.

Ecksteine, C., Bailey, D. G., and Shapiro, A.H., 1977. Self-diffusion of particles in shear flow of a suspension. Journal of Fluid Mechanics 79, 191.

Epstein, N., 2005. Teetering. Powder Technology 151, 2 – 14.

Epstein, N., Pruden, B.B., 1999. Liquid fluidization of binary particle mixtures: III. Stratification by size and related topics. Chemical Engineering Science 54, 401 – 415.

Ergun, S., 1952. Fluid flow through packed columns. Chemical Engineering Progress 48, 89 – 94.

Galvin, K. P., 2003. On the phenomena of hindered settling in liquid fluidized beds, in advances in gravity concentration, Edited by R. Q. Honaker and W. R. Forrest, Published by SME, 19–38.

Galvin, K. P., 2009. Water based fractionation of particles. Chemical Engineering Research and Design 87, 1085 – 1099.

Galvin, K.P., Callen, A., Zhou, J., Doroodchi, E., 2005. Performance of the reflux classifier for gravity separation at full scale. Minerals Engineering 18, 19 – 24.

Galvin, K.P., Dickinson, J.E., 2013. Particle transport and separation in inclined channels subject to centrifugal forces. Chemical Engineering Science 87, 294 – 305.

Galvin, K.P., Doroodchi, E., Callen, A.M., Lambert, N., Pratten, S.J., 2002a. Pilot plant trial of the reflux classifier. Minerals Engineering 15, 19 – 25.

Galvin, K.P., Liu, H., 2011. Role of inertial lift in elutriating particles according to their density. Chemical Engineering Sciences 66, 3687 – 3691.

Galvin, K.P., Nguyentranlam, G., 2002b. Influence of parallel inclined plates on a liquid fluidized bed system. Chemical Engineering Science 57, 1231– 1234.

Galvin, K.P., Swann, R., Ramirez, W.F., 2006. Segregation and dispersion of a binary system of particles in a fluidized bed. AIChE journal 52, 3401 – 3410.

Galvin, K.P., Walton, K., Zhou, J., 2009. How to elutriate particles according to their density. Chemical Engineering Science 64, 2003 – 2010.

Galvin, K.P., Zhou, J., Dickinson, J.E., Ramadhani, H., 2012. Desliming of dense minerals in fluidized beds. Minerals Engineering 39, 9 – 18.

Galvin, K.P., Zhou, J., Walton, K., 2010. Application of closely spaced inclined channels in gravity separation of fine particles. Minerals Engineering 23, 326 – 338.

Horio, M., 2010. Fluidization science, its development and future. Particuology 8, 514 – 524.

Hunter, D.M., Iveson, S.M., Galvin, K.P., 2014. The role of viscosity in the density fractionation of particles in a laboratory-scale Reflux Classifier. Fuel 129, 188–196.

Juma, A. K. A., and Richardson, J. F., 1983. Segregation and mixing in liquid fluidized beds. Chemical Engineering Science 38 (6), 955 – 967.

Kennedy, S.C., Bretton, R.H., 1966. Axial dispersion of spheres fluidized with liquids. A.I.Ch.E. Journal 12, 24.

King, M.R., and Leighton, D.T., 1997. Measurement of the inertial lift on a moving sphere in contact with a plane wall in shear flow. Physics of Fluids 9 (5), 1248 – 1255.

Krishnan, G. P., Leighton Jr, D. T., 1995a. Dynamic viscous resuspension of bidisperse suspensions - I. Effective diffusivity. International Journal of Multiphase Flow 21 (5), 721 – 732.

Kwauk, M., Li, J., Liu, D., 2000. Particulate and aggregative fluidization – 50 years in retrospect. Powder Technology 111, 3 – 18.

Laskovski, D., Duncan, P., Stevenson, P., Zhou, J., Galvin, K.P., 2006. Segregation of hydraulically suspended particles in inclined channels. Chemical Engineering Science 61, 7269 – 7278.

Leighton, D., and Acrivos, A., 1986. Viscous resuspension. Chemical Engineering Science 41 (6), 1377 – 1384.

Leighton, D., and Acrivos, A., 1987a. The shear induced migration of particles in concentrated suspensions. Journal of Fluid Mechanics 181, 415 – 439.

Leighton, D., and Acrivos, A., 1987b. Measurement of shear-induced self-diffusion in concentrated suspensions of spheres. Journal of Fluid Mechanics 177, 109 – 131.

Li, Z., Kobayashi, N., Nishimura, A., Hasatani, M., 2005. A method to predict the minimum fluidization velocity of binary mixtures based on particle packing properties. Chemical Engineering Communications 192, 918 – 932.

Moritomi, H., Iwase, T., and Chiba, T., 1982. A comprehensive interpretation of solid layer inversion in liquid fluidized beds. Chemical Engineering Science 37 (12), 1751 – 1757.

Moritomi, H., Yamagishi, T., Chiba, T., 1986. Prediction of complete mixing of liquid fluidized binary solid particles. Chemical Engineering Science 41, 297 – 305.

Mukherjee, A.K., Mishra, B.K., Kumar, R. V., 2009. Application of liquid/solid fluidization technique in beneficiation of fines. International Journal of Mineral Processing 92, 67 – 73.

Nguyentranlam, G., Galvin, K.P., 2001. Particle classification in the reflux classifier. Mineral Engineering 14, No. 9, 1081-1091.

Patel, B.K., Ramirez, W.F., Galvin, K.P., 2008. A generalized segregation and dispersion model for liquid fluidized beds. Chemical Engineering Science 63, 1415 – 1427.

Pruden, B.B., Epstein, N., 1964. Stratification by size in particulate fluidization and in hindered settling. Chemical Engineering Science 19, 696 – 700.

Ramirez, W.F., Galvin, K.P., 2005. Dynamic model of multi-species segregation and dispersion in fluidized beds. AIChE journal 51, 2103 – 2108.

Rao, B.V., Kapur, P.C., Konnur, R., 2003. Modelling the size–density partition surface of dense-medium separators. International Journal of Mineral Processing 72, 443 – 453.

Rasul, M.G., Rudolph, V., Carsky, M., 2002. Segregation in binary and ternary liquid fluidized beds. Powder Technology 126, 116 – 128.

Rasul, M.G., Rudolph, V., Wang, F.Y. 2000. Particles separation using fluidization techniques. International Journal of Mineral Processing 60, 163 – 179.

Reddy, R.K., Joshi, J.B., 2009. CFD modelling of solid-liquid fluidized beds of mono and binary particle mixtures. Chemical Engineering Science 64, 3641 – 3658.

Richardson, J.F., Zaki, W.N., 1954. Sedimentation and fluidization: Part I. Trans. Instn. Chem. Engrs. 32, 35 – 53.

Rubiera, F., Hall, S.T., Shah, C.L., 1997. Sulfur removal by fine coal cleaning processes. Fuel 76 (13), 1187 – 1194.

Schroen, K., Van Dinther, A., Stockmann, R., 2017. Particle migration in laminar shear fields: A new basis for large scale separation technology? Separation and Purification Technology 174, 372 – 388.

Tripathy, S.K., Bhoja, S.K., Kumar, C.R., Suresh, N., 2015. A short review on hydraulic classification and its development in mineral industry. Powder Technology 270, 205–220.

Van Duijn, G., and Rietema, K., 1982. Segregation of liquid - fluidized solids. Chemical Engineering Science 37(5), 727 – 733.

Wen, C.Y., Yu, Y.H., 1966. A generalized method for predicting the minimum fluidization velocity. A.I.Ch.E. Journal 12, 610 – 612.

Zhang, K., and Acrivos, A., 1994. Viscous resuspension in fully developed laminar pipe flows. International Journal of Multiphase flow 20 (3), 579 – 591.

Zigrang, D.J., Sylvester, N.D., 1981. An explicit equation for particle settling velocities in solid–liquid systems. A.I.Ch.E. Journal 27 (6), 1043 – 1044.